

An integrative model for neuronal activity-induced signal changes for gradient and spin echo functional imaging

Kâmil Uludağ^{*}, Bernd Müller-Bierl, Kâmil Uğurbil¹

Max-Planck Institute for Biological Cybernetics, Hochfeld Magnetresonanz Zentrum, Spemannstr. 41, Tübingen 72076, Germany

ARTICLE INFO

Article history:

Received 10 July 2008

Revised 6 May 2009

Accepted 14 May 2009

Available online 27 May 2009

Keywords:

BOLD signal

fMRI

Gradient-echo

Spin echo

Spatial resolution

High magnetic field

Contrast agent

ABSTRACT

Gradient and spin echo (GRE and SE, respectively) weighted magnetic resonance images report on neuronal activity via changes in deoxygenated hemoglobin content and cerebral blood volume induced by alterations in neuronal activity. Hence, vasculature plays a critical role in these functional signals. However, how the different blood vessels (e.g. arteries, arterioles, capillaries, venules and veins) quantitatively contribute to the functional MRI (fMRI) signals at each field strength, and consequently, how spatially specific these MRI signals are remain a source of discussion. In this study, we utilize an integrative model of the fMRI signals up to 16.4 T, exploiting the increasing body of published information on relevant physiological parameters. Through simulations, extra- and intravascular functional signal contributions were determined as a function of field strength, echo time (TE) and MRI sequence used. The model predicted previously reported effects, such as feasibility of optimization of SE but not the GRE approach to yield larger micro-vascular compared to macro-vascular weighting. In addition, however, micro-vascular effects were found to peak with increasing magnetic fields even in the SE approach, and further increases in magnetic fields imparted no additional benefits besides beyond the inherent signal-to-noise (SNR) gains. Furthermore, for SE, using a TE larger than the tissue T_2 enhances micro-vasculature signal relatively, though compromising SNR for spatial specificity. In addition, the intravascular SE MRI signals do not fully disappear even at high field strength as arteriolar and capillary contributions persist. The model, and the physiological considerations presented here can also be applied in contrast agent experiments and to other models, such as calibrated BOLD approach and vessel size imaging.

© 2009 Elsevier Inc. All rights reserved.

Introduction

Functional magnetic resonance imaging (fMRI) (Bandettini et al., 1992; Kwong et al., 1992; Ogawa et al., 1992) is currently the most popular imaging technique employed for studying brain function non-invasively. The development of fMRI was fueled by the observation of the blood oxygenation level-dependent (BOLD) effect (Ogawa et al., 1990). Underlying this effect are changes in deoxygenated hemoglobin (deoxy-Hb) content resulting from changes in cerebral blood volume (CBV), cerebral blood flow (CBF), and oxygen metabolism following sensory stimulation or cognitive tasks (e.g. Buxton, 2002; van Zijl et al., 1998 and references therein) (see Glossary). Such physiological changes are detectable with MRI because the MR signal is sensitive to microscopic magnetic field gradients. Deoxy-Hb, which is paramagnetic, alters the magnetic susceptibility of blood and creates magnetic field gradients in and

around deoxy-Hb containing blood vessels (Ogawa et al., 1990, 1993; Spees et al., 2001; Thulborn et al., 1982; Weisskoff et al., 1993; Yablonskiy and Haacke, 1994). Functional signals from the brain are encoded simply by a T_2^* or T_2 -weighted gradient recalled echo (GRE) and spin echo (SE) images, respectively. Such images form the basis of the BOLD contrast. However, they also contain neuronal-activity coupled signal alterations originating from mechanisms beyond the BOLD effect.

MRI signals in GRE and SE fMRI arise from intravascular (IV) and extra-vascular (EV) water protons, both of which are dependent on the blood vessel volume and oxygenation as well as on MRI pulse sequence employed. Several imaging parameters, such as echo time (TE), read-out duration, diffusion weighting and field strength, can be selected in order to improve spatial specificity of MRI signals with respect to neuronal activity. The MRI sequence of choice is GRE sequence because it is easy to implement and because of its high Contrast-to-Noise-Ratio (CNR). However, it is generally believed that a single-refocused SE sequence at high but not low magnetic fields yields MRI signals that are spatially more specific because the venous IV signals are diminished at high fields (e.g. Duong et al., 2003; Uğurbil et al., 2003) and the remaining EV signals around large blood vessels are partly re-focused by the additional 180° radio-frequency (RF) pulse employed (Boxerman et

^{*} Corresponding author. Fax: +49 7071 601 702.

E-mail address: kamil.uludag@tuebingen.mpg.de (K. Uludağ).

¹ Current address: Center for Magnetic Resonance Research, Department of Radiology, University of Minnesota Medical School, 2021 6th Street S.E., Minneapolis, MN 55455, USA.

al., 1995a,b; Gilles et al., 1995; Kiselev and Posse, 1999; Kjolby et al., 2006; Weisskoff et al., 1992, 1994; Yablonskiy and Haacke, 1994).

Ideally, fMRI signals should be co-localized with neuronal activity. However, the spatial and physiological specificity of GRE and SE fMRI signals is a complex issue (for a review see Harel et al. (2006b)). Spatial miss-localization can occur due to changes in blood oxygenation and volume in remote draining veins (Frahm et al., 1994; Haacke et al., 1994; Hoogenraad et al., 1999; Kim et al., 1994; Lai et al., 1993; Menon et al., 1993; Oja et al., 1999; Turner, 2002) and due to the different point-spread functions of fMRI signal contributions (Engel et al., 1997; Parkes et al., 2005; Shmuel et al., 2007; Yacoub et al., 2005) as a function of vessel size.

Recently, fMRI at 4.7 T, 7 T and 9.4 T has been used to experimentally investigate the laminar distribution of the BOLD signal in cats and non-human primates in order to test the spatial specificity and the ability of fMRI to resolve functional units (Goense and Logothetis, 2006; Goense et al., 2007; Harel et al., 2006a; Zhao et al., 2004, 2006). The rationale behind this approach is that the neuronal activity and the accompanying hemodynamic changes are not expected to be evenly distributed over the cortical layers. The largest local field potential (LFP), oxidative metabolism changes, neurotransmitter release, and also capillary density are found in layer IV of the cortex (Weber et al., 2008 and references therein). The GRE fMRI signal correlates well with LFP (Logothetis et al., 2001) and, therefore, for sensory stimulation, the fMRI signal should also be highest in this layer. The common finding of these various laminar distribution studies was that GRE fMRI signals, even at high magnetic field strength, peaks at the surface vessels, whereas the fMRI signals obtained using SE peaks also in laminar layer IV (with similar magnitude as surface vessels), demonstrating higher spatial specificity in the later. In one of these studies (Harel et al., 2006a), fMRI was combined with histology, showing an excellent correspondence of cytoarchitecture and the distribution of SE fMRI signal amplitudes.

Other popular test cases to assess the functional specificity of fMRI signals are the detection of ocular dominance columns (ODC) and of orientation columns (OC) in animals and humans. In most mammals, neurons in the primary visual areas preferentially responding to the stimulation of one eye are spatially clustered in ODCs or to one orientation in OCs, respectively. ODCs and OCs have been identified first using the invasive techniques of electrophysiology and optical imaging, and more recently using fMRI non-invasively in animal models (Duong et al., 2001; Moon et al., 2007 and references therein) and in humans (Moon et al., 2007; Yacoub et al., 2007, 2008 and references therein); in the human ODC study, it has also been shown that SE is more specific for such high resolution mapping compared to GRE (Yacoub et al., 2007).

The argument put forward to explain these findings derives from the magnetic field dependence of the venous intravascular contribution and Monte-Carlo simulations of extra-vascular contributions to the BOLD signal. The latter have revealed that, for the same susceptibility value, SE is most sensitive to small vessels (e.g. capillaries) and GRE to large vessels (e.g. draining surface veins) (Boxerman et al., 1995a,b; Gilles et al., 1995; Kiselev and Posse, 1999; Kjolby et al., 2006; Weisskoff et al., 1992, 1994; Yablonskiy and Haacke, 1994). Several fMRI techniques, e.g. the calibrated BOLD approach (Davis et al., 1998) and vessel size imaging (Kiselev et al., 2005), rely on the findings of these simulations.

However, there are several complications that are not fully and/or quantitatively accounted for in these studies. First, the IV contribution to the BOLD signal can be substantial (Obata et al., 2004; van Zijl et al., 1998). This is true especially at low field strengths, where the IV BOLD signal can be as large or larger than the EV BOLD signal (Boxerman et al., 1995a; Jochimsen et al., 2004; Norris et al., 2002; Song et al., 1996). (Note that the notions 'low' and 'high' field strengths are not labeling the field strengths in absolute but in relative terms. In this study, 'low field' labels 1.5 T and 3 T and 'high fields' 7 T and larger.) While largely absent from veins at very high magnetic fields due to the very short T_2 of deoxygenated blood (e.g. Duong et al., 2003 and references therein), IV contributions are conceivable from arterioles where oxygen

extraction is low but not zero, and from capillaries close to their arterial ends where the deoxygenation levels are lower and hence T_2 values are longer (Silvennoinen et al., 2003). Second, for modeling purposes, it is assumed that blood vessels are randomly oriented relative to the external magnetic field which is not necessarily true for surface vessels and cortex-penetrating arteries and veins. Finally, vascular compartments (arteries, arterioles, capillaries, venules, veins) differ in blood oxygenation (Vovenco, 1999) and volume (Weber et al., 2008) and, following functional activation, change their oxygenation values by a different amount. Consequently, the respective relaxation rate changes have to be compared at different susceptibility values. While the arterial and arteriolar effects may be negligible at low magnetic fields, they can become significant at high magnetic fields because the frequency shift across the luminal boundaries of the blood vessels is proportional to the product of the fractional deoxygenation and the static magnetic field magnitude.

In the present study, through simulations, we quantitatively assess the various GRE and SE based fMRI signal contributions and their spatial distribution by using an integrative model for these fMRI signals. The study comprises Monte-Carlo simulations of the extra-vascular BOLD effect, as before, but in addition, incorporation of blood relaxation properties and physiological alterations that accompany neuronal activity changes in a generalized derivation of function-induced signal changes in GRE and SE fMRI. Consequently, GRE and SE fMRI signal changes include the BOLD effect, but also mechanisms that are independent of blood oxygenation changes. Analytical formulae are provided for: a) intrinsic IV and EV relaxation rates (with no deoxy-Hb) derived from published experimental data; b) deoxy-Hb dependence, derived from Monte-Carlo simulations for the EV BOLD signal and for IV BOLD signal from experimental values, and c) contributions of all vascular components from arteries to veins. The model is similar to other previously proposed models (e.g. Buxton et al., 2004; He and Yablonskiy, 2007; Hoogenraad et al., 2001; Lu et al., 2004; van Zijl et al., 1998), but is more comprehensive as it is valid for magnetic field strengths from 1.5 T up to 16.4 T for both GRE and SE. The latter is significant because, as is demonstrated in this study, earlier BOLD modeling results based on simulations covering a smaller range of magnetic fields and/or higher susceptibility differences across blood vessel boundaries cannot be necessarily generalized for higher fields and/or susceptibility gradients, especially for the SE fMRI signals.

We illustrate results obtained with this model for both hyperoxia (i.e. oxygenation change with no CBV change) and functional stimulation. They indicate, most notably, that for SE: a) the IV BOLD signal does not fully disappear for high field strengths but rather shifts to blood vessels with high blood oxygenation; b) diffusion weighting at low field strengths would increase micro-vasculature weighting; c) using a TE larger than the T_2 of tissue also enhances micro-vasculature weighting, although it compromises signal-to-noise ratio in order to gain spatial specificity; d) there is a limit to the magnetic field increases resulting in attaining an improved micro-vasculature weighting; and e) for a hyperoxia experiment, higher micro-vasculature weighting is obtained than for a functional activation experiment. For GRE, there is no field strength at which the BOLD signal in the micro-vasculature is larger than in the macro-vasculature. These results have consequences for assessing spatial specificity of fMRI and for the exact formulation of some standard fMRI techniques currently relying solely on theoretical estimates of EV BOLD signals, e.g. calibrated BOLD signal (Davis et al., 1998) and vessel size imaging (Kiselev et al., 2005).

Theory

Transverse magnetization of nuclear spins decays to zero by processes such as dipole-dipole coupling that is irreversible under a refocusing transformation, as well as dephasing induced by large-scale magnetic field inhomogeneities that is reversible under refocusing. The signal decay is typically characterized by an exponential decay time

constant T_2^* while the irreversible part of the decay is described with the time constant T_2 . The inverse of these time constants are the relaxation rate constants R_2^* and R_2 . If the magnetic field inhomogeneities are on the scale of random thermal motion (diffusion) of the spins, the echo amplitude under a refocusing pulse is also affected. This loss in echo amplitude is often lumped into the T_2 decay even though it cannot strictly be classified as irrecoverable; multiple refocusing pulses, as in a Carr–Purcell pulse train, applied with short intervals in the time scale of thermal motion, will suppress this decrease in echo amplitude. Nevertheless, a loss is encountered due to diffusion in the presence of field inhomogeneities, especially when only one refocusing pulse is often incorporated into the T_2 process, as it is in these simulations.

Both intra- and extra-vascular spins contribute to the total MRI signal S_{tot} (Buxton, 2002; Duong et al., 2003; van Zijl et al., 1998, and references therein). Intra- and extra-vascular MRI signals (S_{in} and S_{ex}) have to be weighted by their respective volumes and, thus, S_{tot} is:

$$S_{\text{tot}} = (1 - \text{CBV}) \cdot S_{\text{ex}} + \sum_i \phi_i \cdot S_{\text{in},i} \cdot \text{CBV}_i \quad (1)$$

The index i denotes the different vascular compartments present in the voxel, i.e. arteries, arterioles, capillaries, venules and veins. Note that, in this equation, CBV is the fractional blood volume in relation to whole tissue volume (typically between 1 to 5% but can also be higher for parenchymal vessels). The term ϕ is the relative proton spin density. Because only signal ratios (e.g., the ratio of the activation/rest signals) will be considered, only a relative scaling of the spin density is required. For this reason, ϕ is defined as the ratio of the IV/EV spin densities and for gray matter, it is slightly larger than one (Lu et al., 2003). However, its value can be decreased by diffusion weighting bi-polar gradient pulses or increased by inflow of unsaturated fresh blood. In the following, we will assume that $\phi = 1$ and omit this variable in the equations below.

The relaxation process of the MR signal is usually described by a single exponential: $S = S_0 \cdot e^{-R_2^* \cdot \text{TE}}$ with S_0 as the effective spin density of the (extrapolated) signal at TE = 0 ms. Note that in this and the following equations, the relaxation rate is R_2 for SE- or R_2^* for GRE-pulse sequence, respectively. The transverse relaxation rate constant $R_2^{(*)}$ is written as the sum of two terms: $R_2^{(*)} = R_{2,0}^{(*)} + R_{2,\text{Hb}}^{(*)}$. Here, $R_{2,0}^{(*)}$ is the intrinsic relaxation value, and $R_{2,\text{Hb}}^{(*)}$ describes the additional relaxation produced by deoxy-Hb. In functional stimulation experiments, the relative contribution of the change in deoxy-Hb to the overall relaxation $R_{2,\text{Hb}}^{(*)}$ is – especially at low field strengths – small compared to the intrinsic $R_{2,0}^{(*)}$ and large-scale field gradients across the voxel. For this reason, the signal changes due to the BOLD effect are typically only in the order of a few percent.

The extra-vascular signal can be written as (Yablonskiy and Haacke, 1994):

$$S_{\text{ex}} = S_0 \cdot e^{-(R_{2,0,\text{ex}} + \sum_i R_{2,\text{Hb},i,\text{ex}}) \cdot \text{TE}} \quad (2)$$

In the following, we ignore the problem of large pial vessels whose extra-vascular effect will be large enough to overlap with those of capillaries, venules, etc. in the adjacent voxel (see Discussion section).

GRE and SE fMRI model for functional activation

During functional activation, changes in both the CBV and the oxygen saturation of hemoglobin Y alter the MR signal. Hence:

$$S_{\text{tot,act}} = (1 - (\text{CBV} + d \cdot \Delta \text{CBV}_{\text{act}})) \cdot S_{\text{ex,act}} + \sum_i S_{\text{in},i,\text{act}} \cdot (\text{CBV}_i + \Delta \text{CBV}_{i,\text{act}}) \quad (3)$$

In this equation, a compression factor d for the extra-vascular volume is introduced, which describes how much the change in blood

volume displaces or compresses the extra-vascular volume, i.e. changes the amount of protons in the extra-vascular space. That is, a value of $d = 0$ implies that the amount of protons in the extra-vascular volume stays the same despite an expansion of blood volume; a value $d = 1$ implies that the increase in the amount intravascular protons is balanced by a decrease in the extra-vascular space either by protons being pushed out of the voxel or displaced into the intravascular space resulting in a constant total amount of protons within the voxel. Because water is not compressible, physiologically, a value close to $d = 1$ is most plausible, and this is assumed in the simulations below.

The BOLD signal change in [%] following neuronal activation is:

$$\frac{\Delta S}{S_{\text{tot}}} = \frac{S_{\text{tot,act}} - S_{\text{tot}}}{S_{\text{tot}}} \quad (4)$$

In sum, to calculate BOLD signal for different vascular compartments, intrinsic relaxation rates without any deoxy-Hb and relaxation rate changes due to deoxy-Hb for both intra- and extra-vascular spins during baseline and functional activation have to be determined. In the following, analytical formulae for each of the BOLD signal contributions are derived from either experimental data or Monte-Carlo simulations.

Intrinsic relaxation rates of tissue

Numerous studies (see Table 1) (e.g. Boxerman et al., 1994, 1995b; Chen et al., 2004; Cremillieux et al., 1998; de Graaf et al., 2006; Deistung et al., 2008; Duong et al., 2002, 2003; Gati et al., 1997; Grabbill et al., 2003; Haacke et al., 2005; Jin et al., 2006; Jochimsen et al., 2004; Keilholz et al., 2006; Lee et al., 1999, 2002; Li et al., 2006; Lu et al., 2007; Lu and van Zijl, 2005; Mitsumori et al., 2007; Peters et al., 2007; Ramani et al., 2006; Spees et al., 2001; Stanisz et al., 2005; Weigel and Hennig, 2006; Yacoub et al., 2003, 2005; Zhao et al., 2004, 2006, and references therein) have measured tissue and blood relaxation rates for both GRE and SE up to field strength of 11.7 T and 9.4 T, respectively. In addition, we performed R_2 relaxation rate measurements at 16.4 T on rat gray matter (unpublished data). Because, typically, the BOLD signal change is only a few percent (avoiding large pial vessels), measured R_2 and R_2^* values in gray matter closely resemble tissue relaxation rates with no deoxy-Hb (see Discussion section for details). Therefore, we take *in vivo* tissue relaxation rates in the presence of deoxy-Hb as representative of tissue relaxation rates with no deoxy-Hb. In Fig. 1a, experimental tissue intrinsic relaxation rates $R_{2,0}$ and $R_{2,0}^*$ taken from the references cited above are plotted.

There is some variation in the values due to experimental error, voxel sizes, brain areas investigated, quality of the shimming, read-out times, species, etc. Both $R_{2,0}$ and $R_{2,0}^*$ increase with field strength possibly due to the inhomogeneous spatial structure of biological tissue. Note that, in contrast, the relaxation rate of pure water has been suggested not to be strongly field strength-dependent (Cremillieux et al., 1998). However, at tissue interfaces, microscopic magnetic field inhomogeneities can be present even though the tissue is on average diamagnetic. Additionally, relaxation rate can be affected by chemical exchange between water protons and macromolecules. Both of these processes probably lead to field strength-dependent relaxation of the intrinsic MR signal (Cremillieux et al., 1998).

Often, functional imaging studies are performed at TE values that approximate gray matter T_2 or T_2^* , e.g. for SE: ~96 at 1.5 T, ~77 ms at 3 T, ~50 ms at 7 T, ~41 ms at 9.4 T, and for GRE: ~66 ms at 1.5 T, ~48 ms at 3 T, ~28 ms at 7 T ~22 ms at 9.4 T (see open circles in Figs. 4 and 5). This condition maximizes stimulus-induced BOLD signal changes and, under the specific conditions where intrinsic thermal noise in an image dominates temporal signal fluctuations in an fMRI time series, also the CNR in both GRE and SE fMRI. Instead of maximizing the BOLD signal change or CNR, however, the choice of TE

Table 1
Experimentally determined tissue relaxation rates for both SE and GRE.

Reference	Field strength [T]	R_2 [1/s]
SE		
Lee et al., 1999	1.5	11.11
	4.7	20
	9.4	25
Stanisz et al., 2005	1.5	10.53
	3	10.1
	3	14
Zhao et al., 2006	1.5	10.11
Duong et al., 2003	3	12.5
	4	15.87
	7	18.19
	9.4	25
	7	20
	1.5	11.1
Jin et al., 2006;	9.4	22
Zhao et al., 2004	3	15.5
Chen et al., 2004	4.7	18.2
Cremillieux et al., 1998	7	23.9
	9.4	22
	1.5	7.94
Weigel and Hennig, 2006	3	8.2
	11.7	26.3
Keilholz et al., 2006	2.35	11.24
Haacke et al., 2005	8.5	23.81
	4	15.34
de Graaf et al., 2006	9.4	23.75
	11.7	27.62
Own observation	16.4	37.3
GRE		
Zhao et al., 2004	7	40
Li et al., 2006	9.4	29.4
	7	27.8
Deistung et al., 2008	1.5	11.9
	3	15.2
	7	30.1
Duong et al., 2003	4	28.6
Lu and van Zijl, 2005	1.5	16.1
Yacoub et al., 2005	3	21.1
	4	24.2
Chen et al., 2004	3	17.8

value may be based on criteria for optimizing the contribution of a specific vascular compartment to the images (see Figs. 4 and 5).

The experimental tissue $R_{2,0}$ data (Fig. 1a) can be fitted with a linear function yielding:

$$R_{2,0,ex} = 1.74 \frac{1}{\text{Tesla} \cdot \text{s}} \cdot B_0 + 7.77 \frac{1}{\text{s}}. \quad (5)$$

Because static magnetic field variations contribute to $R_{2,0}^*$ in addition to processes that contribute to $R_{2,0}$, $R_{2,0}^*$ has to be larger than $R_{2,0}$. Although $R_{2,0}^*$ varies over brain areas and depends on various parameters like voxel size, we linearly fit some of the reported data on $R_{2,0}^*$ and utilize the resultant expression for the simulations. This $R_{2,0}^*$ expression is:

$$R_{2,0,ex}^* = 3.74 \frac{1}{\text{Tesla} \cdot \text{s}} \cdot B_0 + 9.77 \frac{1}{\text{s}}. \quad (6)$$

Intrinsic relaxation rates of blood

There are far fewer studies on blood intrinsic relaxation rate due to difficulties in measuring it *in vivo* or creating a reliable blood phantom. In Fig. 1b, blood relaxation rates for arterial blood with assumed oxygen saturation of $Y = 100\%$ are plotted up to 10 T taken from Lee et al., 1999, Silvennoinen et al. (2003) and Zhao et al. (2007) (and references therein). Note that, for simplicity, intrinsic relaxation rates with no deoxy-Hb for all vascular compartments are assumed to be equal to the arterial relaxation rates, i.e. the different hematocrit values

of blood vessels are ignored. The physical source of the discrepancy of blood R_2^* and blood R_2 is not clear because it is expected that the intravascular protons are in the motional narrowing regime and, thus, both parameters should be similar. However, chemical exchange and microscopic field gradients might again explain this discrepancy.

The experimental intrinsic arterial blood $R_{2,0}$ data (Fig. 1b) can be fitted with a linear function yielding:

$$R_{2,0,in} = 2.74 \frac{1}{\text{Tesla} \cdot \text{s}} \cdot B_0 - 0.6 \frac{1}{\text{s}}. \quad (7)$$

For the $R_{2,0}^*$ curve, no fitting is necessary because at field strengths higher than 4.7 T the blood contribution using GRE sequences is

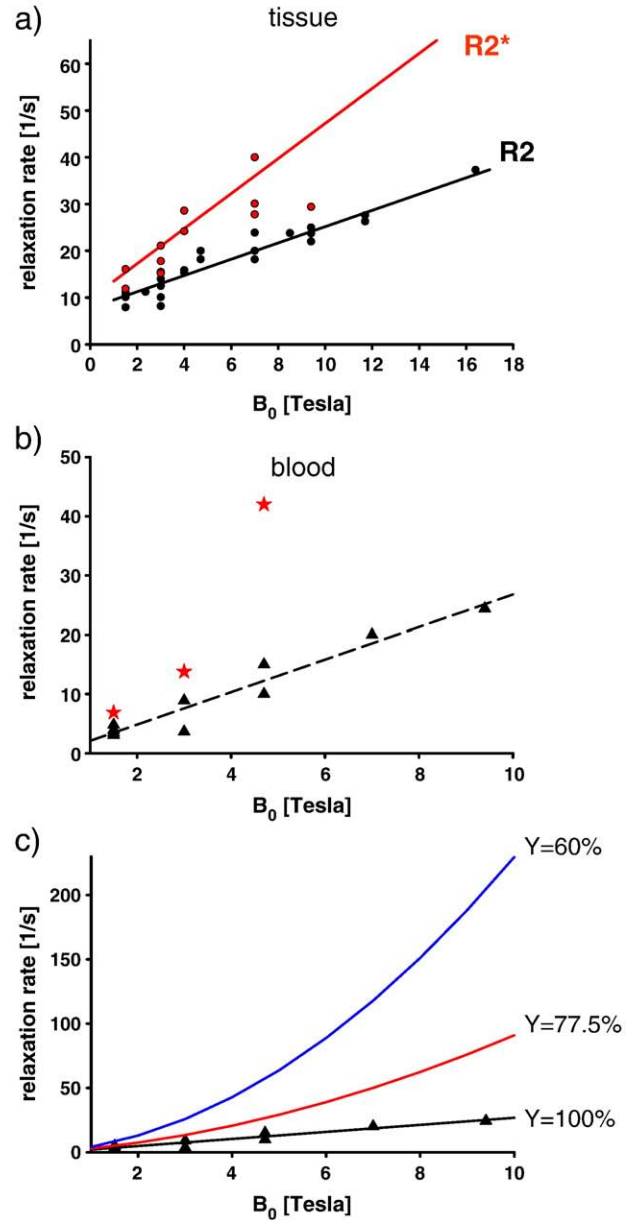


Fig. 1. a) Intrinsic tissue relaxation rate (i.e. for oxygen saturation $Y = 100\%$) for GRE (red) and SE (black) as a function of magnetic field strength B_0 . Experimental data are shown with dots and fitted curves with lines. **b)** Intrinsic blood relaxation ($Y = 100\%$) for GRE (red) and SE (black) as a function of magnetic field strength B_0 . For display purposes, only up to $B_0 = 10$ T is plotted. **c)** Blood relaxation rate for SE for different blood oxygenation values. $Y = 100\%$ (black) corresponds to intrinsic blood relaxation rate shown in b). Relaxation rates increase with field strength. Intrinsic relaxation rates of tissue for SE and fully oxygenated blood are comparable in magnitude whereas blood relaxation is significantly higher for oxygen saturation much lower than 100%.

negligible due to high relaxation rates (see Fig. 1b). For 1.5 T, 3 T and 4.7 T, the arterial relaxation rate values can be taken directly from Fig. 1b and, for 4 T, the value can be linearly interpolated between 3 T and 4.7 T, yielding a relaxation rate of 30.4 s^{-1} .

For SE, intrinsic relaxation rates of arterial blood and tissue are similar. As a consequence, contrary to venous blood where the blood MRI signals disappear at high magnetic field, signals from fully oxygenated arterial blood or blood with small amounts of deoxy-Hb (found in arteries, arterioles and beginning sections of the capillaries) will persist (see Figs. 3 and 4) even at a high field. This is not to be confused, however, with the venous blood contribution, which dominates the BOLD effect at low field strengths, but which rapidly decreases with increasing magnetic fields due to strong field dependence of blood T_2 caused by the presence of large amounts of deoxy-Hb. If a CBV change is ignored, blood signals can contribute to the BOLD effect only when the T_2 or T_2^* of blood changes with neuronal activity alterations. This occurs only in sections of the vasculature where oxygen extraction occurs and downflow sections that drain these vessels. Oxygen extraction typically occurs in capillaries but some also exists in arterioles as well. However, with a CBV change, all vascular compartments can contribute to the GRE or SE fMRI signals; strictly speaking then, these fMRI signals will not just be BOLD signal, since the BOLD effect refers to the consequences of blood oxygenation.

Intravascular relaxation rate as a function of oxygen saturation using blood phantom data

As mentioned above, the IV water is much closer to the source of the paramagnetic inhomogeneity and, thus, it is more sensitive to the presence of deoxy-Hb than the EV signal. Few attempts have been made to numerically calculate IV relaxation rates for 1.5 T (e.g. Boxerman et al., 1995a; Gilles et al., 1995). Fortunately, using blood phantoms, the relaxation rate as a function of deoxy-Hb can experimentally be determined and, at 1.5 T, 3 T and 4.7 T, this was done most comprehensively by van Zijl and colleagues (Silvennoinen et al., 2003; Zhao et al., 2007). In the following, the quadratic fit on the experimental data for SE presented in these papers with no linear component was taken (i.e. $R_{2,\text{in}} = C \cdot (1 - Y)^2 + A$). Thus, for the quadratic dependence of the relaxation rate on blood de-oxygenation, the following values were adopted: for 1.5 T: $C = 21 \text{ s}^{-1}$, for 3 T: $C = 125 \text{ s}^{-1}$ and 4.7 T: $C = 254 \text{ s}^{-1}$. For simplicity, we took only the results at one hematocrit (Hct) value (Hct = 0.44 at 1.5 T and 4.7 T and 0.4 at 3 T). (Note that the constant A is equal to the intrinsic relaxation rate $R_{2,0}$ (i.e. relaxation rate of fully oxygenated blood) in Fig. 1b and Eq. (7).)

In contrast, at 9.4 T Lee et al. (1999) found a linear relationship between SE relaxation rate and blood de-oxygenation. However, quadratic dependence of the relaxation rate changes on de-oxygenation is also expected at 9.4 T: The relaxation rate depends quadratically on the chemical shift which in turn depends linearly on the magnetic susceptibility difference between the red blood cells and blood plasma and, thus, the amount of deoxy-Hb. From the data shown in Fig. 2 in the paper of Lee et al., and a forced quadratic dependence on de-oxygenation, relative to $Y = 100\%$, the factor $C = 1125 \text{ s}^{-1}$ is obtained. Using the same argument, a quadratic dependence on the magnetic field strength is also predicted, for example, by the Luz–Meiboom exchange model (Duong et al., 2003; Jensen and Chandra, 2000). Thus, a quadratic fit on the factors C at different field strengths yields for $R_{2,\text{Hb},\text{in}}$ data:

$$R_{2,\text{Hb},\text{in}} = \frac{12.67}{\text{Tesla}^2 \cdot \text{s}} \cdot B_0^2 \cdot (1 - Y)^2. \quad (8)$$

(Note that, the total intravascular relaxation rate $R_{2,\text{in}}$ is equal to $R_{2,0,\text{in}} + R_{2,\text{Hb},\text{in}}$ with $R_{2,0,\text{in}}$ given in Eq. (7)). In Fig. 1c, resulting

SE blood total relaxation rates for arterial ($Y = 100\%$), capillary ($Y = 77.5\%$, taken as an average over the capillary) and venous ($Y = 60\%$) are plotted, for display purposes, only up to 10 T. The plot for $Y = 100\%$ is the experimental data that is already presented in Fig. 1b.

The presented empirical model of IV BOLD signal differs from the Luz–Meiboom exchange model in two ways: a) the intrinsic relaxation rate $R_{2,0,\text{in}}$ (Fig. 1b) is field strength-dependent; and b) relaxation rate is mono-exponential (i.e. relaxation rate constant itself is not TE-dependent). Clearly, more experimental data on blood relaxation rates at different oxygenation levels and field strengths are needed.

For GRE, IV relaxation rate dependence on oxygenation, an analytical formula only up to 4.7 T is needed (Silvennoinen et al., 2003; Zhao et al., 2007) because the blood signal for all vascular compartments is decayed away for realistic TE

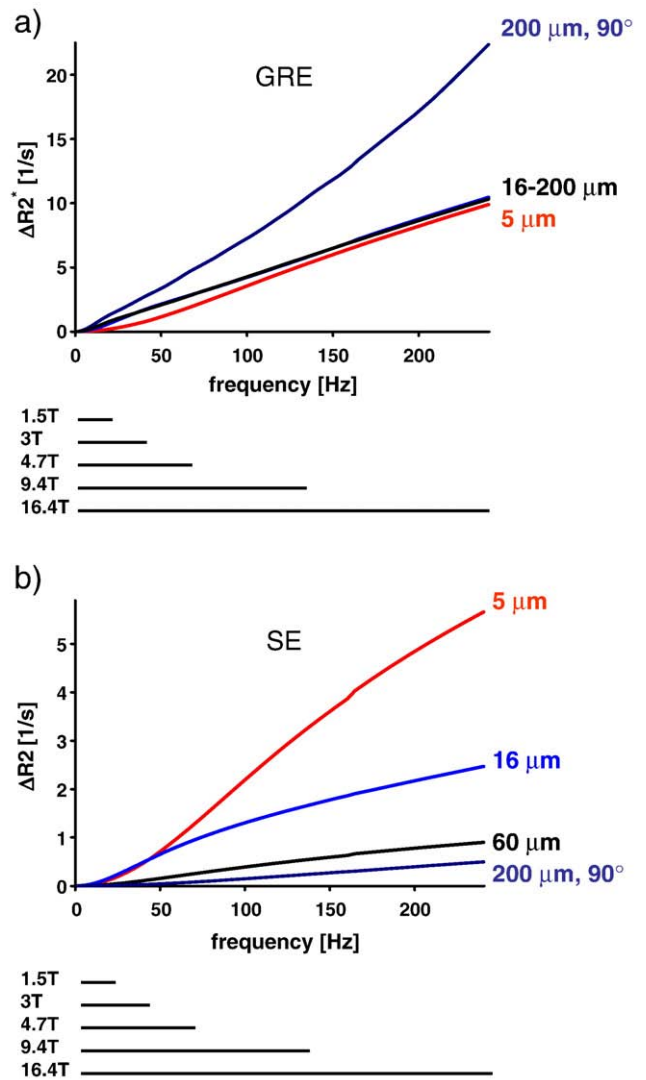


Fig. 2. Monte-Carlo simulation results for tissue relaxation rate for different cylinder diameters for both a) GRE and b) SE as a function of frequency on the surface of the cylinder $\Delta\nu_s$. The frequency $\Delta\nu_s$ is proportional to de-oxygenation and field strength. The lines below the graph depict the ranges of frequencies for $Y = 95\%$ to 45% for each field strength. The relaxation rate is the average of the relaxation rates of randomly oriented cylinders and is given per % of CBV. Additionally, the relaxation rate for a cylinder with diameter = 200 μm oriented perpendicular to the magnetic field is shown (dark blue line).

values at high field strengths. For 4 T, the coefficient was linearly interpolated.

$$R_{2,\text{Hb},\text{in}}^* = 25 \cdot (1 - Y)^2 \text{ (1.5T)} \quad (9a)$$

$$R_{2,\text{Hb},\text{in}}^* = 181 \cdot (1 - Y)^2 \text{ (3T)} \quad (9b)$$

$$R_{2,\text{Hb},\text{in}}^* = 262 \cdot (1 - Y)^2 \text{ (4T, interpolated)} \quad (9c)$$

$$R_{2,\text{Hb},\text{in}}^* = 319 \cdot (1 - Y)^2 \text{ (4.7T)}. \quad (9d)$$

Extra-vascular relaxation rate as a function of oxygen saturation using Monte-Carlo simulation

Water molecules undergo random motion and, thus, molecules starting at the same location will spread out over time experiencing the magnetic field gradients created by a paramagnetic substance, e.g. deoxy-Hb, around a vessel. The spatial scale of the field gradient is proportional to the vessel radius. Without diffusion, each spin remains at the same location, and precesses in the same field offset for the entire duration till echo time TE. In this case, the distribution of phases is directly proportional to the distribution of field offsets (designated the 'static dephasing'-regime). In the limiting case of very rapid diffusion, each spin wanders around the vessel, sampling the full range of field offsets (designated the 'motional narrowing'-regime). This reduces the phase dispersion because all the spins have similar phase histories regardless of their starting location at $t = 0$. In short, diffusion moderates the effects of the field offsets, so the GRE signal is most attenuated for the static dephasing regime and much less attenuated for the motional narrowing regime. If field distortions are on a small enough scale, then diffusion becomes important, the 180° RF pulse in a SE sequence does not fully refocus the signal, and there is attenuation of the SE signal. In contrast, the EV signal around big vessels is re-focused by the 180° RF pulse employed.

To the best of our knowledge, there is currently no quantitative *in vivo* experimental method to determine quantitatively for each vascular compartment (arteriole, capillary ...) separately their extra-vascular contributions and relaxation rates as a function of oxygen saturation. Thus, several papers have been published determining these functions using computer simulations (Bandettini et al., 1995; Boxerman et al., 1995a,b; Fisel et al., 1991; Fujita, 2001; Gilles et al., 1995; Hoogenraad et al., 2001; Ogawa et al., 1993; Weisskoff et al., 1992, 1994). The modeling results have partially been validated using polystyrene microspheres or by comparison with the analytical formulae derived for slow ('static dephasing') and fast diffusion ('motional narrowing') regimes (Boxerman et al., 1995a; Boxerman et al., 1995b; Gilles et al., 1995; Kiselev and Posse, 1999; Kjolby et al., 2006; Weisskoff et al., 1992, 1994; Yablonskiy and Haacke, 1994).

The Monte-Carlo algorithm used in this study is similar to the previously employed simulations to determine extra-vascular signals mentioned above. Consequently, similar results were obtained, whenever comparable susceptibility values and diameters for GRE or SE were used (e.g. Ogawa et al., 1993; Boxerman et al., 1995a; Fujita, 2001). Briefly, in an infinite cylinder with a volume fraction a certain CBV was assumed. It was shown previously, and confirmed by our simulations, that relaxation rates are simply proportional to CBV within the range of physiologically plausible CBV values. The field distribution for the magnetic field outside the vessel can analytically be calculated. The susceptibility-induced shift at the surface of the vessel corresponds to a Larmor frequency shift $\Delta\nu_s$ given by:

$$\Delta\nu_s = \frac{\Delta\chi_0}{4 \cdot \pi} \cdot \text{Hct} \cdot (|Y_{\text{off}} - Y|) \cdot \gamma \cdot B_0. \quad (10)$$

$\Delta\chi_0 = 4 \cdot \pi \cdot 0.264$ ppm is the susceptibility of blood with fully deoxygenated blood, $\text{Hct} = 40\%$, and $\gamma = 2\pi \cdot 42.6$ MHz/T is the

gyromagnetic ratio of protons. Note that a value of $4 \cdot \pi \cdot 0.264$ ppm for $\Delta\chi_0$ was recently experimentally determined (Spees et al., 2001) and differs from the value of $4 \cdot \pi \cdot 0.18$ and $4 \cdot \pi \cdot 0.31$ ppm used in earlier studies. Y_{off} is the O₂ saturation that produces no magnetic susceptibility difference between intravascular and extra-vascular fluids, and is usually assumed to be one, as it was in earlier studies. However, the intrinsic susceptibility of the extra-vascular space was recently also reported to be the same as plasma for $Y_{\text{off}} = 0.95$ (Spees et al., 2001). This value was adopted in this study. Weisskoff and Kiihne (1992) even found a value of $Y_{\text{off}} \sim 0.8$. Note that using other values for $\Delta\chi_0$ and Y_{off} would result in a different $\Delta\nu_s(Y_{\text{off}}, B_0)$ function than utilized here. However, the results were not found qualitatively to be sensitive to the exact value of $\Delta\chi_0$, demonstrating similar trends with respect to the dependence on the magnetic field magnitude. Quantitatively, there were significant differences in the magnitude of the effects calculated, as would be expected. For example, the magnitude of the spin-echo fMRI signal at 7 T changed from ~2% to ~3% to ~3.5% when $\Delta\chi_0$ was varied from $4 \cdot \pi \cdot 0.18$ to $4 \cdot \pi \cdot 0.264$ to $4 \cdot \pi \cdot 0.31$, respectively, for the case where the CBV change was taken to be zero (data not shown).

Nine different vessel orientations relative to the direction of the main magnetic field (θ : 10°, 20°, 30°, 40°, 50°, 60°, 70°, 80°, and 90°) were modeled and the results were added, weighted by the frequency of their appearance in a randomly oriented vessel network (same orientational weighting as in Ogawa et al. (1993):

$$S = \frac{\sum_{\theta} S(\theta) \sin(\theta)}{\sum_{\theta} \sin(\theta)}.$$

At each time step, stochastically-distributed protons moved the distance $\ell = \sqrt{6D\Delta t}$ in a random direction. $D = 1 \mu\text{m}^2/\text{ms}$ is the diffusion coefficient for water in brain parenchyma (Le Bihan, 2003). Diffusion was limited to the EV space which is physiologically plausible given that the exchange time of water between EV and IV spaces is thought to be ~500 ms (Eichling et al., 1974; Paulson et al., 1977). Depending on the local magnetic field, a magnetization phase was added at each time step. This procedure was repeated until the TE was reached. For SE, the phase values of the proton spins were inverted at TE/2.

The signal decay was approximated with a mono-exponential function within the interval from 16 to 40 ms (Ogawa et al., 1993). It was previously reported that the initial part of the decay deviates from a mono-exponential curve (e.g. see Yablonskiy and Haacke, 1994; Kiselev and Posse, 1999; Fujita, 2001). Our simulations confirmed this observation and also demonstrated that this deviation is larger for SE than for GRE, increases with vessel diameter and diminishes with increasing field strength. The mono-exponential fit and the real signal decay of the EV signal as a function of oxygenation can largely be matched to each other for different TE values. That is, on a logarithmic scale, the fit and the real decay are just shifted versions to each other. Thus, using a mono-exponential approximation instead of the real decayed signal value results in an error of using a longer TE in the simulations for EV signal compared to calculation of the IV signal. However, the consequent error only results in small amplitude changes for both micro- and macro-vasculature EV BOLD signal and, thus, has a minor effect on the general results. For 7 T, for example, the values for micro- and macro-vasculature were 2.2% and 1.2%, respectively, using the mono-exponential approximation and 2.05% and 1.05% using the real signal decay. Thus, the ratio of micro- vs. macro-vasculature remains relatively unaffected. Given the uncertainties in the other values for the estimation of the EV signal, e.g. diffusion constant, average vessel orientation, vessel size, and the relative small consequence of the mono-exponential assumption, in the simulations presented in this paper, the mono-exponential approximation of the signal decay is used as it allows deriving an expression for the EV relaxation rate.

The modeling was performed for cylinders with diameters ranging from 2 to 200 μm . The results are plotted only for diameters = 60–200 μm (black), 16 μm (blue) and 5 μm (red) (Figs. 2a and b). In this figure, the horizontal axis is a measure of the susceptibility difference between the extra- and intravascular spaces, expressed as the susceptibility-induced frequency change, $\Delta\nu_s$, on the vessel wall surface. Note that relaxation rates for diameters between 16 to 200 μm are almost identical for GRE but not for SE and, therefore, only one GRE curve is shown representing all diameters within this range. Except for small offset frequency values, the relaxation rates for SE function of frequency offset obey the power law with the exponent 2/3 as described in Kiselev and Posse (1999).

The assumption of random orientation is not true for larger vessels, as surface vessels and tissue-penetrating arteries and veins are oriented along one direction. To estimate the *upper limit* of the effect of oriented vessels on BOLD signals, we report also extra-vascular signal changes for 90° oriented blood vessels relative to the main magnetic field B_0 with diameter = 200 μm (dark blue) (Fig. 2).

For GRE, the enhancement of the relaxation rate of extra-vascular protons due to increasing $\Delta\nu_s$ (Eq. 10) is larger for large and medium (diameter 16–200 μm) sized vessels compared to small (5 μm diameter) vessels (Fig. 2a). For 5 μm diameter vessels, the increase in the relaxation rate with $\Delta\nu_s$ is non-linear initially as previously shown by modeling studies, but at high $\Delta\nu_s$ values it also becomes approximately linear and comparable to the relaxation rate of larger vessels. For SE, the contribution to the extra-vascular relaxation rate from blood vessels with diameter greater than 16 μm tends to level off with increasing $\Delta\nu_s$ whereas it continues to increase for 5 μm diameter blood vessels (Fig. 2b). However, even for 5 μm diameter blood vessels, the increase in R_2 with increasing $\Delta\nu_s$ starts leveling off at very high $\Delta\nu_s$. All curves in Fig. 2 can be fitted by polynomials of fifth or lower orders (see Table 2):

$$R_{2,\text{Hb,ex}}^{(*)} = (a \cdot \Delta\nu_s^5 + b \cdot \Delta\nu_s^4 + c \cdot \Delta\nu_s^3 + d \cdot \Delta\nu_s^2 + e \cdot \Delta\nu_s + f) \cdot \text{CBV}_i \quad (11)$$

(For GRE, analytical expressions for EV relaxation rates for medium and large vessel sizes have been developed, see for example Yablonskiy and Haacke (1994), similar in values to the results from our Monte-Carlo simulations except for small susceptibility values.) The biggest effect on the EV BOLD signal for GRE is from the large vessels oriented perpendicularly to the main magnetic field; also, the slope is higher for this vessel type and orientation. For SE, the slope is highest for the 5 μm diameter vessels.

The $\Delta\nu_s$ values in Fig. 2 (horizontal axis) do not directly correspond to the magnetic field magnitude for all blood vessels. This is because different vessel types will not all have the same deoxy-Hb content and hence $\Delta\nu_s$ *in vivo* at the same time, except for the post-capillary venules and veins. Deoxy-Hb content increases going from arteries, arterioles, capillaries, venules to veins (e.g. decreased oxygen saturation $Y = 100\%$, 95%, 77.5% (averaged over its length), 60%, and 60%, respectively). Thus, for a given magnetic field, the higher $\Delta\nu_s$ values have to be used the further downstream the blood vessel is.

Results

Physiological assumptions for the illustrations

In order to determine baseline and activation-induced intra- and extra-vascular signals of each vascular compartment using the equations given above, blood volume fractions and oxygenation values have to be assumed. The exact values for volume and oxygenation are currently a matter of intense research. Recently, the capillary CBV fraction in the blood volume in the tissue (excluding pial vessels) in the macaque visual areas was determined to be approximately 40% (Weber et al., 2008) and we assume that venules occupy twice the volume as arterioles. In the same study, total CBV in the tissue (again excluding large pial vessels) was found to be between 2 and 2.5%.

Thus, for the following illustrations, the micro-vasculature is defined as having a blood volume of $\text{CBV}_{\text{micro-vasculature}} = 2.5\%$ consisting of arterioles ($20\% \cdot \text{CBV}_{\text{micro-vasculature}}$), capillaries ($40\% \cdot \text{CBV}_{\text{micro-vasculature}}$) and venules ($40\% \cdot \text{CBV}_{\text{micro-vasculature}}$). For simplicity, we assume a single diameter for each vessel type (see Figs. 2a and b): $d_{\text{capillary}} = 5 \mu\text{m}$; and $d_{\text{arteriole/venule}} = 16 \mu\text{m}$. The diameter we take for capillaries is in exact agreement with the diameter of 5.1 ± 0.81 reported by Pawlik et al. (1981) in the cat cortex. For GRE, the exact value of arteriole/venule diameter is not very important as the EV BOLD signal is relatively insensitive to the diameter (see Fig. 2a) much beyond the capillary scale. For SE, however, a larger average diameter yields a decrease in the EV BOLD signal contribution of this vessel type (see Fig. 2b) (see Discussion section). In our definition of the micro-vasculature, intracortical arteries and veins (with typically diameters of 20 to 120 μm) that run perpendicular to the cortex are excluded since they degrade the local specificity of the BOLD signal as oxygenation changes in one layer propagates into another layer via these vessels (Duvernoy et al., 1981).

To estimate the relative BOLD signal magnitude of a draining vein within or on the surface of the cortex (i.e. BOLD signal due to macro-vasculature) was defined as originating from a $d = 200 \mu\text{m}$ vein and oriented orthogonal to B_0 (see Figs. 2a and b) and assumed to have a larger blood volume value of $\text{CBV}_{\text{vein}} = 5\%$. Note that, in order to determine the maximal effect of macro-vasculature, in contrast to the micro-vasculature which is randomly oriented, the vein is taken to be orthogonally oriented to the external magnetic field. Experimentally, the exact values of CBV for micro- and macro-vasculature will depend on voxel size and position (e.g. partial voluming with white matter and CSF).

For baseline oxygen saturation, following Vovenko (1999), average saturation values of $Y_{\text{arteriole}} = 95\%$, and $Y_{\text{venule}} = Y_{\text{vein}} = 60\%$ and $Y_{\text{capillary}} = (Y_{\text{arteriole}} + Y_{\text{venule}}) / 2 = 77.5\%$ were chosen. (Note that arterial oxygenation is 100% but arteriolar oxygenation during baseline is assumed to be 95% throughout the entire text.) In the capillaries, we approximated the progressive decline in blood oxygenation level from the arteriole down to the venous oxygenation state with the average of these two values. Similarly, the low level oxygen extraction that exists at the arteriolar level would lead to a gradient along the length of the arteriole, which is also approximated by a single average value. During

Table 2
Fitting coefficients for a polynomial of 5th order for the various vessel diameters for both GRE and SE shown in Figs. 2a and b.

$R_{2,\delta}^{(*)} = (a \cdot \Delta\nu_s^5 + b \cdot \Delta\nu_s^4 + c \cdot \Delta\nu_s^3 + d \cdot \Delta\nu_s^2 + e \cdot \Delta\nu_s + f) \cdot \text{CBV}_i$	a [s^4]	b [s^3]	c [s^2]	d [s]	e	f [1/s]
HSE 5 μm	−1.13e−11	0.96e−8	−3.22e−6	4.90e−4	−3.58e−3	0.0175
HSE 16 μm	−1.92e−11	1.26e−8	−2.89e−6	2.51e−4	0.0067	−0.0382
HSE 60 μm	−4.61e−12	3.15e−9	−8.08e−7	9.13e−5	2.11e−4	−2.22e−3
HSE 200 μm , 90°		1.47e−10	−9.77e−8	2.41e−5	−1.10e−4	4.91e−4
GRE 5 μm		5.04e−9	−3.05e−6	6.17e−4	−8.02e−4	−0.005
GRE 16–200 μm			−3.56e−6	−3.56e−6	0.0453	−0.194
GRE 200 μm , 90°		−8.76e−10	7.29e−6	−3.42e−5	0.0717	−0.166

functional activation, oxygenation values change to: $Y_{\text{arteriole}} = 100\%$, $Y_{\text{venule}} = Y_{\text{vein}} = 70\%$ and $Y_{\text{capillary}} = (Y_{\text{arteriole}} + Y_{\text{venule}}) / 2 = 85\%$. Note that, given the Eqs. (1–11), results for voxel blood volume composition and oxygenation values other than those used in the illustrations below can easily be calculated.

The BOLD signal change is modeled for an oxygenation change accompanied either by a CBV change in the micro-vasculature or without a CBV change. Because we want to determine an upper estimate of the effect of the draining vein effect and because CBV increase leads to a decrease in BOLD signal, no CBV change of the large vein is assumed. Although pial vessels do show some CBV change, in studies with the intravascular contrast agent MION, CBV change measured in layer IV, attributed to micro-vascular CBV change, was found to be larger than the CBV change in surface vessels (Smirnakis et al., 2007; Yacoub et al., 2006; Zhao et al., 2006). For simplicity, in each vascular compartment of the micro-vasculature, the same fractional CBV change of 16.6%, as suggested previously by Vanzetta et al. (2005), is assumed, corresponding to a 50% blood flow change under Grubb's law (Grubb et al., 1974).

The cases without a CBV change correspond physiologically to hyperoxia experiments as it was suggested that even 100%-O₂ hyperoxia would only decrease CBF by maximally 10% (Chiarelli et al., 2007). During functional experiments, it was proposed that CBV change occurs mostly in arteries/arterioles (Duong and Kim, 2000; Kim et al., 2007). Because the arteriole contribution to the BOLD signal is actually small (see red curves in figures below), both scenarios (hyperoxia with no CBV change or CBV change dominated by the arteries/arterioles) would yield similar results.

Illustrations

Given these assumptions, Figs. 3a and b plot the intra- and extra-vascular fMRI signal contributions for a vein (200 μm, 90° relative to B₀, the maximum effect), arterioles (16 μm), capillaries (5 μm) and venules (16 μm) without (dashed lines) and with (solid lines) a CBV change for SE at TE equal to tissue T₂ (T_{2,tissue} values are indicated by the open circles in Figs. 5a and b) as a function of magnetic field strength. The higher the field strength, the shorter is the TE employed. Here and in the following, the calculations were performed for 1.5 T, 3 T, 4 T, 4.7 T, 7 T, 9.4 T, 11.7 T and 16.4 T.

A CBV increase has the effect of increasing the amount of protons in the blood vessels and, hence, a larger IV fMRI signal increase. In the following, if not otherwise stated, the results given in brackets are without a CBV change (dashed lines). For field strengths <7 T [or <8 T], the largest IV fMRI signal for the SE (Fig. 3a) contribution comes from the vein. Please note that the vein contribution does not have a solid line plot in this figure, since, for this vessel size, no volume change was assumed. In the micro-vasculature consisting of arterioles, capillaries and venules, the capillary IV fMRI contribution is greatest for field strengths larger than 3 T [4 T]. Note that there is also a non-negligible IV fMRI contribution for arterioles. At field strengths up to 5 T, the total IV fMRI signal (see also Fig. 3c) is dominated by veins and, thus, an increase of capillary and overall micro-vasculature weighting can be achieved by using diffusion gradients. One must be aware, however, that using diffusion weighting at 1.5 T might result in a total fMRI signal that is too small to be detected as previously shown experimentally (Boxerman et al., 1995a; Song et al., 1996).

In Fig. 3b, the EV fMRI signal contributions for SE are plotted. In the following, tissue fMRI signal is defined as the total fMRI signal without any IV contribution, i.e. it takes into account both the change in EV relaxation rate and the amount of protons left in the tissue compartment of the voxel as a consequence of the CBV change (see below). That is, tissue fMRI signal as defined here is total EV BOLD signal multiplied by (1 – CBV) (see Eqs. (1) and (3)). Note that the scaling in Fig. 3b is larger than in Fig. 3a. A CBV increase (solid lines) decreases the tissue fMRI signal because of the (1 – CBV) terms as the

amount of protons in the extra-vasculature is decreased. The capillaries are the largest tissue BOLD contributor in the micro-vasculature for >5 T [>7 T]. For lower field strengths, venules contribute most to the MRI signal. The arterioles contribute negatively to the BOLD signal because its baseline oxygenation (Y=95%) is chosen to be the same as the oxygen saturation for which there is no susceptibility effect in the EV volume.

Total IV signals relative to the total fMRI signal for SE for micro-vasculature only, macro-vasculature only and both together are plotted in Fig. 3c (with CBV change, solid lines in Figs. 3a, b). Note that not only the IV signal but also the total fMRI signal is calculated from contributions for micro-vasculature only, macro-vasculature only and both together. With increasing field strength, the IV contribution is between 94% and 98% at 1.5 T and decreases to a value between 7% and 11% at 16.4 T. Interestingly, the relative IV contribution is not very sensitive to the vascular composition.

The total fMRI signal of the micro-vasculature (black lines) in SE approximately doubles with the field strength (Fig. 3d) (solid line) and levels off after ~7 T in the presence of a CBV increase, while it continues to increase when CBV remains unaltered in this compartment (dashed line). This strong effect of CBV on the field dependence of the SE microvascular contribution to functional signals comes from two effects. First, as in GRE, increasing CBV means an increase in the total amount of deoxy-Hb in the voxel leading to decreased effective T₂ in the extra-vascular space and hence a decrease in EV BOLD and a decrease in function-induced signal change. However, there is a second, more significant, mechanism operational. Namely, when CBV increases, tissue water decreases and the blood water increases, with the total amount of water in the voxel staying constant. However, this conservation of mass is not applicable to the MR signal. While the decrease in tissue water content corresponds to a decrease in tissue water signals, increase in blood volume does not have a commensurate compensation at high fields. As the field increases, the blood water signals in deoxy-Hb containing vasculature decay more rapidly relative to the tissue signals due to their ever shortening T₂ with increasing magnetic field. In other words, the displacement and consequent loss of tissue signal due to an increase in CBV is magnetic field independent when data are acquired at TE approximately equal to tissue T₂. But, the corresponding increase in IV signals from the increased CBV is field dependent, especially for capillaries and post-capillary vessels, and decreases with increasing magnetic field (Fig. 3a) when TE ≈ tissue T₂ and longer than the blood T₂. At the extreme condition, when the blood signals of deoxy-Hb containing compartments virtually vanish due to this T₂ decay even in the functionally activated state, this effect becomes analogous to the VASO mechanism (Lu et al., 2003). In VASO, the IV signal is intentionally nulled using an inversion pulse and an appropriate delay subsequently, so that an increase in function-induced CBV simply leads to a decrease in extra-vascular signal without a commensurate increase in blood signals. The same effect happens naturally at high enough fields even without the inversion pulse to actively suppress the blood signals when the deoxy-Hb containing blood T₂ is sufficiently shortened relative to the tissue T₂ even in the activated state. Thus, at high fields, the CBV increase counteracts the signal change that originates from EV BOLD due to the elevation in oxygen saturation with increased neuronal activity.

The impact of this mechanism, therefore, will strongly depend on where the CBV increase takes place. In these simulations, when the CBV increase is considered, it is assumed to affect capillary, arteriole and venule components. If the CBV increase is mainly arteriolar, as previously suggested (Kim et al., 2007), then the capillary and venule contribution will follow more the dashed lines in Figs. 3a,b,d instead of the solid lines. A similar cancellation effect is not operative for these calculations in the macro-vascular contribution because for these calculations, CBV was assumed to be constant.

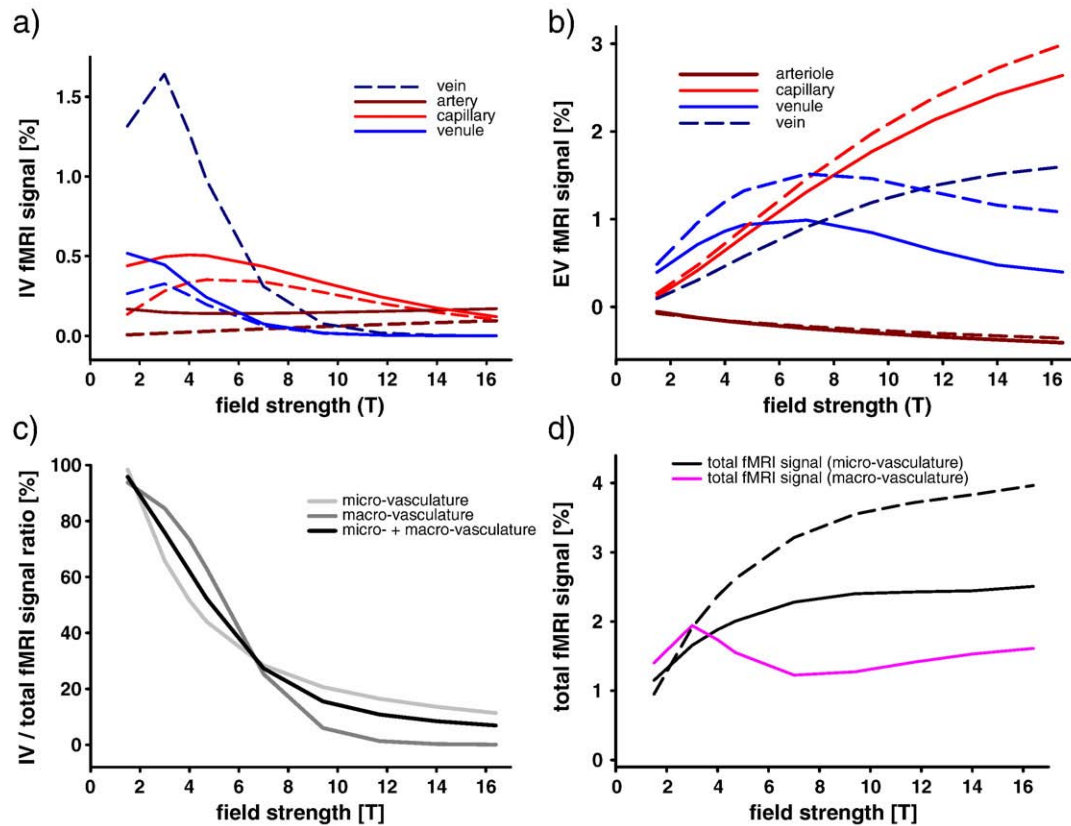


Fig. 3. Simulation results for SE fMRI and echo time $TE = T_{2,tissue}$ as a function of field strength: a) Intravascular (IV) signal contributions for arteriole (brown), capillary (red), venule (light blue) and vein (dark blue) with (solid lines) and without (dashed lines) a cerebral blood volume (CBV) change. b) Extra-vascular (EV) MRI signal for the various vascular compartments. c) IV fMRI signal relative to the total fMRI signal for micro- (light gray), macro- (dark gray) vasculature or both together (black). d) Total fMRI signal for micro- (black) and macro-vasculature (pink).

With or without a micro-vascular CBV change, the micro-vascular SE fMRI signal is significantly larger than the macro-vascular SE fMRI signal for >4 T and >3 T, respectively (Fig. 3d). The total SE fMRI signal of the macro-vasculature (pink line) has a local minimum at about 8 T, mainly due to the vanishing intravascular contribution (Fig. 3a), and increases due to extra-vascular effects with further increases in field strength. Because of this, an increase in magnetic field strength beyond a certain value does not necessarily imply a larger relative micro-vasculature weighting (see Fig. 4). When comparing the micro- vs. macro-vascular ratio, it should be remembered that the macro-vascular contribution was considered under conditions that maximize it, namely a blood vessel with a 90° orientation to the static field, twice as much blood volume as the micro-vasculature, and no CBV change.

The relative BOLD contribution of the micro- vs. macro-vasculature can be changed by altering TE. In Figs. 4a and b, the ratio of micro- vs. macro-vasculature is shown as a function of TE and field strength for the case without (Fig. 4a) and with (Fig. 4b) a CBV change for SE fMRI. Red colors indicate a higher relative micro-vasculature contribution; blue colors a lower relative micro-vasculature contribution. Tissue T_2 values are indicated by open circles. In general, micro-vasculature vs. macro-vasculature weighting is increased for $TE > T_{2,tissue}$ (except for 16.4 T). Note, however, that a larger TE value is associated with a lower SNR value; therefore, the optimum TE for micro-vasculature weighting might not always be recommendable in a real fMRI experiment. There is a maximum of micro-vasculature weighting between 4 T and 9 T and $TE > T_{2,tissue}$. At 7 T, for example, an increase of TE by 20 ms increases the relative micro-vasculature weighting by 50% (Fig. 4a). As argued above, a CBV change has a negative contribution to the tissue fMRI signals and we assumed no CBV change in the macro-vasculature. The relative micro-vasculature contribution is smaller

when a CBV change only in this compartment but not in the macro-vasculature is assumed (Fig. 4b).

In Figs. 5a and b, the EV fMRI and total fMRI signals for GRE at optimum TE with and without CBV changes are plotted. For all field strengths, the macro-vasculature dominates over the micro-vasculature significantly. In Fig. 5c, the ratio of the IV fMRI signal relative to the total fMRI signal is shown. It is zero for field strengths larger than 4.7 T as even the arterial IV signal is decayed away at optimum TE (see Fig. 1b). The minimum value of relative IV fraction for GRE fMRI signal is determined by the macro-vasculature and the maximum by the micro-vasculature. For micro-vasculature, the model predicts a relative IV contribution to the total GRE fMRI signal of $\sim 57\%$ at 1.5 T. For 3 T, 4 T and 4.7 T the relative IV contribution is 36%, 11% and 5%, respectively, if only micro-vasculature is considered. For macro-vasculature, the values at 1.5 T, 3 T, 4 T and 4.7 T are: 11%, 11%, 3% and 1%. Fig. 5d is plotted in the same way as Fig. 4b, but for GRE instead of SE. Note that the color scaling is different in this figure. As can be seen, for GRE sequences, there is no TE value at any field strength for which a higher micro-vasculature than macro-vasculature weighting is achieved. Although the general conclusions would not be altered for GRE fMRI signals, again it should be remembered that the macro-vascular effects were calculated under conditions that maximize them and will not be applicable for all voxels *in vivo*.

Discussion

Different water (proton) pools inside blood vessels and in tissue contribute to the total MRI signal. How the different sources add both intrinsically and as a function of blood oxygenation and volume, and how their relative fractions change with magnetic field or spin preparation is a complex subject. Here, we describe a quantitative

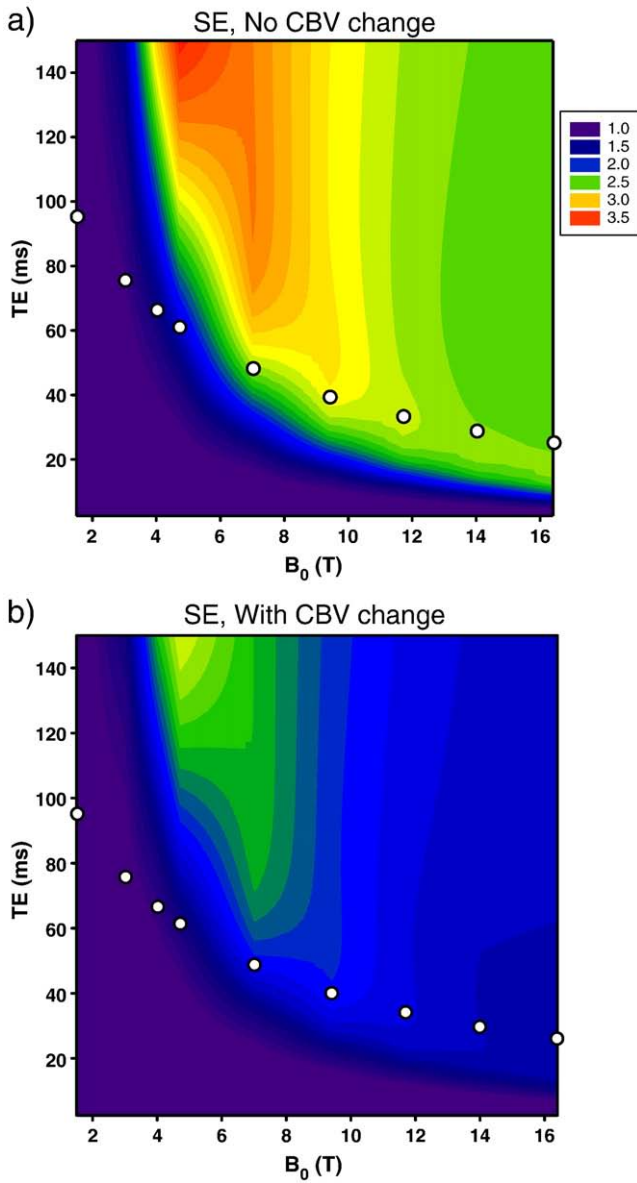


Fig. 4. a) For SE, ratio of micro- vs. macro-vasculature as a function of both TE and magnetic field strength without a CBV change. Open circles indicate tissue T_2 . b) is same as a) but with a CBV change. Color scale indicates the ratio of the SE fMRI signal changes of micro- vs. macro-vasculature. Red colors indicate higher micro-vasculature contribution; blue colors a lower micro-vasculature contribution. Highest micro-vasculature contribution is for field strengths between ~ 4 and ~ 9 T and for $TE > T_{2,tissue}$.

integrative model of the fMRI signal by providing expressions for IV and EV relaxation rates for GRE and SE sequences up to 16.4 T with no deoxygenated hemoglobin and as a function of blood oxygenation and volume. These formulae were derived from published experimental data and, for the oxygenation dependence of the overall fMRI signal ascribed to the EV BOLD mechanism, from Monte-Carlo simulations. This integrative model of the BOLD signal was applied on hyperoxia and functional stimulation to investigate the effects of different contributions to the fMRI signal and its spatial specificity.

Micro- vs. macro-vasculature

In general, there is no parameter set (e.g. TE, main magnetic field strength) for which GRE fMRI is weighted more towards micro- than macro-vasculature (see Fig. 5). However, for SE, for field strengths larger than 3 T, strong micro-vascular weighting can be achieved (see Fig. 4). It was found that the largest micro-vascular weighting is for

field strengths between 4 T and 9 T. The reasons for the maximal micro-vasculature specificity between 4 T and 9 T are: i) the IV signal of veins enhances the macro-vasculature weighting at field strengths < 5 T (see Fig. 3a) and ii) at a very high field strength, for which the EV BOLD signal contributes most to the total fMRI signal, the EV BOLD signal for large veins and capillaries increases proportionally (see Fig. 3b). The reason for this is that while at lower fields, the capillary EV BOLD effect is in the fast diffusion averaging limit, and hence increases supralinearly, at very high magnetic fields this is no longer the case; instead, as in large vessels, even the capillary EV BOLD effect becomes approximately linearly dependent on the field strength, as can be seen in Figs. 2a and b. At first glance, the latter observation seems to contradict earlier results (e.g. Ogawa et al., 1993) predicting a quadratic dependence on oxygenation for capillaries and linear dependence for larger vessels. This apparent discrepancy is due to the smaller range of frequency differences induced by the susceptibility gradient values used in earlier studies: for the same susceptibility value range, identical results are in fact obtained. In addition, using $TE > T_2$ of tissue increases micro-vasculature weighting which is due to larger IV than tissue relaxation rates.

These results are in good agreement with experimental data described previously investigating laminar specificity of the fMRI signals at 4.7 T, 7 T and 9.4 T showing that for GRE fMRI signals peak at surface vessels whereas SE fMRI peaks also in laminar layer IV (Goense and Logothetis, 2006; Goense et al., 2007; Harel et al., 2006a; Zhao et al., 2004, 2006). However, one recent study even showed that fMRI signal maxima, albeit not a very steep one, in middle laminar layers is observable in humans at 3 T using a surface coil and multi-shot segmented GRE imaging allowing high spatial resolution (~ 0.6 mm isotropic voxels) whilst conserving the read-out and echo time necessary for optimal BOLD contrast (Ress et al., 2007). This is quite surprising, because in the animal studies described above and also in the model, GRE sequences showed a surface vessel weighting even at higher field strength. The animal model studies, however, also indicate that if the region of cortical surface is avoided, an fMRI signal maximum in the middle layers can be detected. Thus, one possible reason to have achieved laminar resolution with GRE sequence at 3 T is that the authors used high resolution isotropic voxels reducing partial volume effects with veins, and careful non-standard analysis, as well as possibly avoiding cortical surface region with large pial vessels.

In addition, the integrative model predicts that, for SE, in a hyperoxia experiment (i.e. oxygenation change with no CBV change) a higher micro-vasculature weighting is obtained than in a functional activation experiment (i.e. oxygenation change accompanied by a CBV change) (see Figs. 3 and 4). This follows immediately from the assumption that the CBV change occurs in micro-vasculature; this decreases the tissue volume and hence the tissue contribution to the overall signal of that voxel when blood T_2 is less than the tissue T_2 . This contribution is of opposite sign compared to the EV BOLD signal due to increased oxyhemoglobin content of the blood induced by hyperoxia. In addition, increased CBV itself has a negative effect on the EV BOLD mechanism, which reduces the EV BOLD contribution that is attained simply by decreasing deoxy-Hb concentration in the blood without an accompanying CBV increase. Hyperoxia predominantly changes oxygenation whereas functional stimulation acts on both oxygenation and volume. That is, when comparing hyperoxia with functional stimulation, one can experimentally determine the laminar spatial location of the largest CBV change during functional activation. In addition, the prediction that the micro- vs. macro-vasculature ratio and therefore the laminar distribution changes with TE can be experimentally tested. However, to the best of our knowledge, this has not yet been done systematically.

Nonetheless, one should be aware that the discussion of relative contribution of micro- and macro-vasculature does not address the question of physical point-spread-function (PSF) of MRI (e.g. Shmuel et al., 2007). In order to study PSF of GRE and SE at each field strength, MRI signal changes in one voxel created by a vessel which is located in

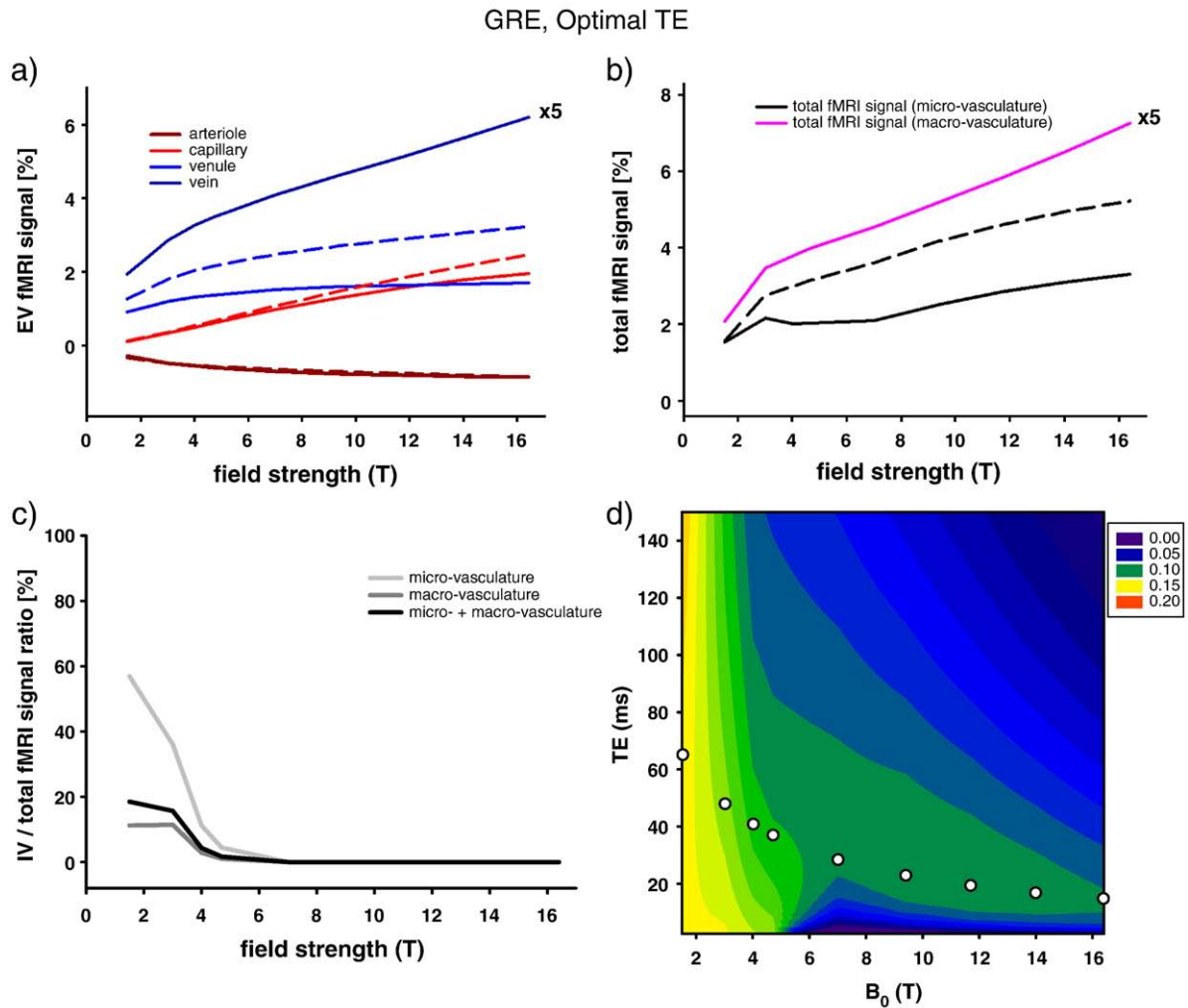


Fig. 5. Simulation results for GRE and $TE = T_{2*}^{\text{tissue}}$ as a function of field strength: a) EV fMRI signal for arteriole (brown), capillary (red), venule (light blue) and vein (dark blue) with (solid lines) and without (dashed lines) a CBV change. b) Total fMRI signal for micro- (black) and macro-vasculature (pink). Note that, for better visibility, the EV and total fMRI signal of the veins in a) and b) have been rescaled by a factor of 5. c) IV fMRI signal relative to the total fMRI signal for micro- (light gray), macro- (dark gray) vasculature or both together (black). d) Ratio of micro- vs. macro-vasculature as a function of both echo time TE and magnetic field strength. Open circles indicate tissue T_{2*}^{tissue} .

a different voxel have additionally to be determined. This is beyond the scope of the present study. Currently, we are trying to answer this question using a one-cylinder and realistic vessel architecture model.

Intra- vs. extra-vascular

As mentioned above, the IV signal can experimentally be attenuated by employing diffusion-weighting bi-polar gradients (Boxerman et al., 1995a; Duong et al., 2003; Le Bihan, 2003; Lee et al., 1999, 2002; Song et al., 1994, 1995, 2003). At relatively low b -values typically employed in BOLD studies, the intravascular signals are suppressed or even eliminated due to inhomogeneous blood flow within the blood vessel and, in the case of the micro-vasculature, random orientation of different blood vessels. The higher the b -value of the gradients, the lower would be the requirement of flow inhomogeneity within a vessel or within a voxel to suppress the flowing spins. Thus, the amount of suppressed IV signal will depend on the b -value and the blood volume composition determined by the voxel position. The experimental values must therefore be regarded as lower estimates of the IV contribution because not all of the IV signal may have been destroyed by the diffusion weighting gradients. In some studies, a range of b -values were employed, leading to an assessment of how complete the suppression of intravascular signals was. A further complication comes from the fact that diffusion-

weighting gradients also suppress inflow effects in fMRI signals. Without an independent assessment of this effect or experimental conditions where such inflow effects are diminished or even eliminated, diffusion-weighting studies would tend to overestimate the blood contribution. As a consequence, a rigorous comparison of modeling data with experimental data is not feasible and the comparisons must remain qualitative.

Our integrative GRE fMRI model predicts that, for macro-vasculature (vein oriented orthogonal to the main magnetic field and at twice the CBV volume as micro-vasculature), the EV BOLD signal using GRE sequence dominates at all field strengths. Therefore, the relative IV contribution is very low (see Fig. 5a). For micro-vasculature, the model predicts a relative IV contribution to the total GRE BOLD signal of ~57%, 36%, 11% and 5% at 1.5 T, 3 T, 4 T and 4.7 T, respectively (see Fig. 5c) for $TE = T_{2*}^{\text{tissue}}$. That is, the minimum value of relative IV fraction for GRE BOLD signal is determined by the macro-vasculature and the maximum by the micro-vasculature.

These theoretical predictions can qualitatively be compared with previously published experimental findings. fMRI diffusion-weighted experiments at 1.5 T using GRE have shown that at least 2/3 of the fMRI signal change is of intravascular origin (Boxerman et al., 1995a; Lu and van Zijl, 2005; Song et al., 1996), which lies close to the maximum value predicted by the model. For GRE at 4 T and 7 T, little or no suppression of the total MRI signal by diffusion weighting was

observed at long TE values and this observation was independent of b -values in the range 0 to 500 s/mm² (Duong et al., 2003). This indicates that negligible IV signal was present in GRE fMRI when long TEs were employed at each field strength (55 ms at 7 T and 80 ms at 4 T) (Duong et al., 2003). However, such long TE values are not typically used for gradient echo experiments at these field strengths. Nevertheless, they do demonstrate that at such long TE values, intravascular signals are virtually eliminated at these magnetic fields in GRE studies, consistent with the predictions of our simulations.

With respect to IV contributions obtained using a SE sequence, the focus has been in venule and vein contribution with the largest deoxy-Hb effect. This contribution increasingly diminishes at high magnetic fields, as expected (see Fig. 3a). However, this does not necessarily mean that the total IV contribution disappears with increasing field strength. Instead, as indicated by our simulations (see Fig. 3a), the IV BOLD signal from blood vessels with high blood oxygenation (arterioles, capillaries) persists (Silvennoinen et al., 2003). This, however, is not detrimental to spatial specificity of SE fMRI. While IV contributions from veins are expected to degrade spatial specificity, capillary blood contributions, and to a lesser extent arteriolar contributions, will certainly be more spatially specific.

There are considerably more experimental studies examining the IV contribution in SE BOLD-based fMRI signals. The relative IV contribution to the total SE fMRI signal is less sensitive to the vascular composition (i.e. the voxel's position) than GRE (see Fig. 3c). For SE at 3 T, half of the BOLD signal has experimentally been found to arise from IV (Norris et al., 2002) of which 30–40% stems from the microvasculature (Jochimsen et al., 2004); from the model, the IV contribution to the total SE fMRI signal is expected to be slightly higher. This is consistent with the experimental data because it is likely that vascular signals were not completely eliminated by the b -value employed (see Fig. 3c). At 4 T and 7 T for TE = 32 ms, ~70% and ~20%, respectively, of the total SE fMRI signal could be suppressed with diffusion gradients (Duong et al., 2003); again, this is in agreement with the predictions of our simulations. At TE = 65 ms and 55 ms, respectively, diffusion weighting could only suppress 20% of the SE fMRI signal even at very high b -values at both field strengths indicating that the IV signal had already decayed away at these TE values; these results, however, were obtained on 2 subjects. A more detailed follow-up study with eight subjects and 16 measurements by the same group later reported essentially identical results at 7 T, but with a somewhat greater blood contribution relative to the total function-induced signal change at 4 T (~40%) when TE was equal to tissue T_2 (Yacoub et al., 2003). This is in agreement with our simulations.

The study by Yacoub et al. (2003) presented detailed experimental data on activation-induced percent signal change as a function of TE for SE fMRI, with and without diffusion gradients, and at 4 T and 7 T. This large body of experimental data can accurately be predicted from our model with excellent quantitative agreement (Fig. 6). Using the model presented in the current study, we have calculated the TE dependence of the total fMRI signal with and without IV contributions and in the presence of a micro-vascular CBV increase at both 4 T and 7 T (see Fig. 6a). This should be compared with Fig. 2 in Yacoub et al. (2003), with total fMRI signals with and without IV contribution corresponding to experimentally measured percent changes with and without diffusion weighting gradients, respectively. In general, the experimental data and the modeling predictions are in excellent agreement. The only difference is the zero intercept of the experimental data without the diffusion weighting gradients both at 4 T and 7 T. This non-zero positive intercept can arise from the presence of significant inflow effects and from a TE-independent, T_2^* contribution coming from the EPI k -space coverage, and was ascribed to these effects by Yacoub et al. Naturally, neither of these experimental problems is present in the modeling data. The diffusion weighting gradients will abolish the inflow effect but not the T_2^* in the experimental study. In the presence of the diffusion weighting

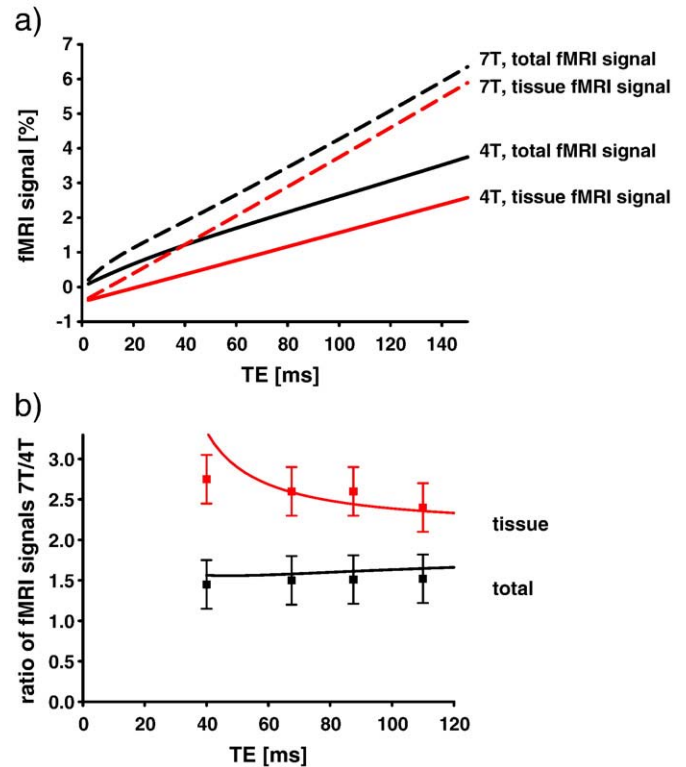


Fig. 6. a) For SE, tissue (red line) and total (tissue and intravascular signals together, black line) fMRI signal as a function of TE for 4 T (solid lines) and 7 T (dashed lines). Negative intercept of tissue fMRI signal indicates the effect of CBV-induced reduction of water molecules in the extra-vascular space as in the VASO effect (Lu et al., 2003). Diverging tissue and total fMRI signals indicate the significant presence of blood signals at 4 T and less so at 7 T. b) Ratio of SE fMRI signal at 7 T vs. 4 T as a function of TE with (black line) and without (red line) inclusion of intravascular signals, predicted from the model. Also shown are the experimental values (squares) taken from Fig. 3 in Yacoub et al. (2003) obtained from the visual cortex during photic stimulation with and without diffusion weighting (i.e. with and without suppression of the IV signals, respectively), showing excellent agreement with modeled data. The 7 T/4 T SE fMRI signal ratio for both cases, i.e. with and without diffusion weighting, is almost independent of TE in this TE range with diffusion weighting resulting in higher ratios due to higher IV contribution at 4 T.

gradients (i.e. no IV contribution), however, the model would predict a negative intercept that is independent of the field strength. This negative intercept comes from the displacement and hence the reduction of the tissue signals in the voxel by the expanding vascular space which, however, is devoid of any signals when the IV contribution is eliminated, i.e. the VASO like mechanism previously discussed (Lu et al., 2003). This is exactly what is observed in the experimental data. Furthermore, the magnitude of this negative intercept as a % signal change should simply be equal to the product of the fractional increase in CBV and the CBV/(tissue volume) ratio. In our modeling, this is approximately -0.4% , again, in excellent agreement with the experimental data in Fig. 2 shown in Yacoub et al. (2003). Thus, assigning the positive non-zero intercept of the SE fMRI signals in the absence of diffusion weighting in Yacoub et al. (2003) to largely inflow effects that would be eliminated with diffusion weighting yields excellent quantitative agreement with the modeling results.

Among the interesting features that are predicted by the model (Fig. 6a) and experimentally observed (Fig. 2 in Yacoub et al. (2003)) is the fact that for 7 T but not for 4 T, the difference between the diffusion-weighted ($b = 100$ s/mm²) vs. non-weighted ($b = 0$ s/mm²) data were approximately the same at all TE values greater than approximately 40 ms to 50 ms. This is expected when blood signals are already negligible at TE of 40 ms to 50 ms or longer, which is

expected for 7 T but not for 4 T. In Fig. 6b, the ratio of the total SE fMRI signal at 7 T vs. 4 T predicted from our model with (red line) and without (black line) diffusion weighting, i.e. without and with IV signal, respectively, is depicted as a function of TE. For TE <40 ms, there is a singularity when the diffusion-weighted BOLD signal at 4 T is zero; thus, the plot is only shown for values TE >40 ms. Also shown in this figure are the experimental values taken from Fig. 3 in Yacoub et al. (red and black squares corresponding to without and with diffusion weighting, respectively). The agreement between the model and experimental data is excellent, especially without diffusion weighting when the IV signals are included in the total fMRI signals. The ratio for both cases with and without diffusion weighting is quite insensitive of TE and, because of larger IV signal contribution at 4 T compared to 7 T, diffusion weighting increases this ratio. The results also illustrate that in the 4 T to 7 T range, when the blood contribution is suppressed, the SE fMRI signals increase supra-linearly approaching the quadratic range predicted for microvasculature. Beyond this field strength, however, the field dependence of the increase is not as steep according to our simulations. This remains to be tested experimentally.

Our modeling results are also consistent with the suggestion that diffusion weighting can improve spatial specificity. For magnetic field strength lower than 5 T, the IV BOLD signal contribution of the vein for SE is predicted to be larger than of venules and capillaries together; therefore, a diffusion weighting yields a larger micro-/macrovasculature ratio in the total BOLD signal (see Figs. 3a and 4a).

In summary, a comparison of the experimental diffusion-weighted results for both GRE and SE with the predictions of our simulations yields a good agreement between them. However, experimental data on fMRI signals with and without diffusion weighting at various field strengths are sparse. Thus, more data systematically testing the relative IV contribution at various field strengths for both GRE and SE as a function of the voxel's blood volume composition is needed to further validate the theoretical model.

An interesting incidental finding of the model is that the EV BOLD signal of the arterioles is negative. The reason for this effect is that at baseline oxygenation values of arterioles ($Y=95\%$), there is no magnetic susceptibility difference between blood plasma and tissue (see Spees et al. (2001)). Therefore, an increase of the arteriolar oxygen saturation to 100% creates susceptibility difference between blood and tissue, thus decreasing the BOLD signal. This effect potentially contributes to the so-called 'initial dip' undershoot (for an overview see Buxton (2001) and Ugurbil et al. (2003)). However, this notion remains to be experimentally tested. These conclusions would of course quantitatively change if the susceptibility difference between fully deoxygenated blood and tissue is taken to be different from the value we have employed based on the data by Spees et al. (2001).

Limitations of the modeling

In our modeling, baseline oxygenation values and blood volume fractions and their respective changes during hyperoxia and functional stimulation have to be assumed, which were physiologically motivated: baseline oxygenation values were derived from Vovenco (1999), baseline total and capillary CBV from Weber et al. (2008) who studied the primate visual cortex. However, the exact values depend on species, brain regions, physiological state, partial volume effects with cerebrospinal fluid and white matter. Note that, nevertheless, given the Eqs. (1–11), results for other voxel blood volume composition and oxygenation values can easily be calculated.

There are some limitations to the model to be mentioned. The equations for the tissue and blood intrinsic relaxation rates were derived from experimental data. However, very little published data is available at high field strengths, and the experimental results that are available are quite variable, resulting in some differences between data obtained from the fit and experimental data for a given field

strength. For example, the T_2 for tissue was reported to be 55 ms for 7 T (Yacoub et al., 2003), but from the fit of all available T_2 data we obtained a T_2 of 45 ms for 7 T and used this for the calculations (e.g. see Figs. 4 and 5); future studies will hopefully improve the accuracy of these expressions. In addition, in deriving the Eqs. (7–9a–d) for blood relaxation rates as a function of oxygenation, we had to rely on only a few studies (Lee et al., 1999; Silvennoinen et al., 2003; Zhao et al., 2007). Here, again, more studies, especially at high magnetic field strengths, are needed to validate the expressions given here. Moreover, for the IV signal, we have taken the values for the relaxation rate for one hematocrit value (Silvennoinen et al., 2003; Zhao et al., 2007) and ignored changes in hematocrit during oxygenation changes. However, using different hematocrit values for each vascular compartment and including hematocrit changes has only a minor effect on the results and, qualitatively, does not alter the conclusions (data not shown). The IV relaxation rates have been taken from blood phantom or sample measurements. It is not clear how representative these values are given that blood vessels are organized in a random network. Theoretically, for GRE, the issue of changing relaxation properties by a random network has been investigated by Sukstanskii and Yablonskiy (2001).

Furthermore, the intrinsic tissue relaxation rates (Fig. 1a) were taken from measured total MRI relaxation rates (excluding pial vessels) instead of, ideally, from tissue with 100% blood oxygenation. Numerical estimation yields that this error in intrinsic tissue relaxation rate is maximally at 16.4 T and is 10% (data not shown). Given the uncertainties in the experimental values and subject, brain area and scanner variations, thus, this approach yields valid estimation of intrinsic tissue relaxation rates.

In addition, for simplicity, only one average diameter of the vessel representing each vessel type was used. However, in the modeling, we calculated the relaxation rates for diameters between 2 and 200 μm and can provide these data to interested readers. For the EV BOLD signal using GRE, this assumption has little impact because different vessel sizes have similar relaxation rates (see Fig. 2a), except for low main magnetic field strength. For the EV BOLD signal using SE, the relaxation rates depend more on vessel size. Using, for example, an average vessel diameter larger than 16 μm for the venules decreases the EV BOLD signal contribution of this vessel type significantly. Furthermore, the oxygenation gradient in blood vessels and blood volume variation along the vessel were also ignored.

Finally, the diffusion in the EV space was isotropic which, however, is not exactly correct due to inhomogeneous cell-compartmentalization of the tissue and the complications on water diffusion presented by cell membranes are not accounted for. However, the diffusion constants used for the simulations correspond to average diffusion constants experimentally recorded where the impact from these problems also exists. To our knowledge, the inhomogeneous structure, and transmembrane exchange of water in the tissue were not taken into account by any numerical simulations of the EV BOLD signal thus far published. In addition, He and Yablonskiy (2007) have suggested that two tissue compartments have to be included into the modeling of the EV BOLD signal. Because both tissue compartments have been suggested to have substantially different baseline relaxation values, the impact of the second compartment is probably small for the functional changes in the range of TE investigated.

The assumption was made that the amplitudes of the different signal sources are additive. However, due to the magnetization phase difference of tissue and blood vessels, the different signals have to be summated in a vectorial fashion (Hoogenraad et al., 2001). Note, though, that this assumption is also made in most of the BOLD models (Buxton et al., 2004; Duong et al., 2003; van Zijl et al., 1998). What is the impact of this simplification? For SE, the impact of this effect on the total fMRI signal is probably low because the static phase difference between blood and tissue is re-focused by the 180° RF pulse. Therefore, only the small phase difference

changes between tissue and blood following activation have to be considered and can be assumed to be small. For GRE, the situation is more complicated as no re-focusing RF pulse is used. Boxerman et al. (1995a) have found that the phase difference does not play a large role for the fMRI signal change at 1.5 T for GRE. However, because the phase difference is proportional to the main magnetic field strength, this might not be true at high field strengths. In a random network, like the micro-vasculature, the impact of the phase difference between blood and tissue will, for the most part, average out. However, for a large vessel with a single orientation, the phase difference will also be large. Because the IV signal disappears at high field strength, therefore, we speculate that the phase difference effect will not change the fMRI signal significantly at high fields. Furthermore, very large pial vessels for which magnetic field disturbances extend significantly into neighboring voxels were not considered in the current study. In summary, based on these arguments, the phase difference in tissue and veins affecting local relaxation rate might play a role in MR phase images but a small role in functional stimulation experiments depending on the magnetic field strength, which, however, has to be tested and incorporated in a refined model.

Finally, no inflow effects were considered in the illustrations which, however, can easily be incorporated by changing the IV signal contributions with values of $\phi > 1$ (see Eq. (1)). Moreover, signal relaxation during the read-out window has been neglected. This can also easily be integrated using the equations given above and incorporating an additional mono-exponential T_2^* -decay in k-space during the read-time window. Essentially, this would result in GRE weighting of the SE signal. Furthermore, scanning parameters affecting the amplitude of S_0 , e.g. TR and flip angle, were not considered. For short TR and differences in blood and tissue T1, the modeling above has to be modified as the images will have a T1 weighting in addition to T_2^* -weighting. Lastly, the current simulations have ignored the consequences of the presence of CSF or white matter in a given voxel. If the relaxation properties of these contributions differ significantly from that of gray matter, especially for CSF, partial voluming with these compartments will modify the results. The impact of the differences in relaxation rates can be determined by using intrinsic relaxation rates of CSF or white matter instead that of gray matter (given in Eqs. (5–6)).

Conclusion

In summary, an integrative model of the BOLD signal up to 16.4 T for GRE and SE is provided. For both IV and EV BOLD signals, expressions for intrinsic relaxation rates and as a function blood oxygenation and volume were derived from experimental and computer simulation data. The model was illustrated using oxygenation and volume values typical for micro- and macro-vasculature derived from experimental data (Vovenko, 1999; Weber et al., 2008). It was found that IV and EV signal contributions vary with field strength, echo time, diffusion weighting and MRI sequence used, and that these imaging parameters can be optimized to yield high micro-vasculature weighting of the fMRI signal. The model presented in this study can also be applied to determine the fMRI signal contributions for GRE and SE in contrast agent experiments. Finally, due to the fact that some MRI approaches are solely based on the EV signal dependence on oxygenation, e.g. calibrated BOLD signal (Davis et al., 1998) and vessel size imaging (Kiselev et al., 2005), these models have to be revised based on the model provided in this study.

Acknowledgments

We thank Essa Yacoub and Anne-Catherin Zappe for comments on an earlier version of the manuscript, and Peter van Zijl for discussion. This work was supported by the Max Planck Society.

References

- Bandettini, P.A., Wong, E.C., Hinks, R.S., Tikofsky, R.S., Hyde, J.S., 1992. Time course EPI of human brain function during task activation. *Magn. Reson. Med.* 25, 390–397.
- Bandettini, P.A., Boxerman, J.L., Davis, T.L., Wong, E.C., Weisskoff, R.M., Rosen, B.R., 1995. Numerical simulations of the oxygenation dependence of the T2 and T2* of whole blood using a deterministic diffusion model. Third Meeting, Society of Magnetic Resonance, Nice, France, p. 456.
- Boxerman, J.L., Weisskoff, R.M., Kwong, K.K., Davis, T.L., Rosen, B.R., 1994. The intravascular contribution to fMRI signal change. Modeling and diffusion-weighted in vivo studies. Proc. SMR, 2nd Meeting, San Francisco, p. 619.
- Boxerman, J.L., Bandettini, P.A., Kwong, K.K., Baker, J.R., Davis, T.L., Rosen, B.R., Weisskoff, R.M., 1995a. The intravascular contribution to fMRI signal change: Monte Carlo modeling and diffusion-weighted studies in vivo. *Magn. Reson. Med.* 34, 4–10.
- Boxerman, J.L., Hamberg, L.M., Rosen, B.R., Weisskoff, R.M., 1995b. MR contrast due to intravascular magnetic susceptibility perturbations. *Magn. Reson. Med.* 34, 555–566.
- Buxton, R.B., 2001. The elusive initial dip. *NeuroImage* 13, 953–958.
- Buxton, R.B., 2002. Introduction to Functional Magnetic Resonance Imaging: Principles and Techniques. Cambridge University Press, Cambridge.
- Buxton, R.B., Uludağ, K., Dubowitz, D.J., Liu, T.T., 2004. Modeling the hemodynamic response to brain activation. *NeuroImage* 23 (Suppl 1), S220–233.
- Chen, N.K., Oshio, K., Panych, L.P., Rybicki, F.J., Mulkern, R.V., 2004. Spatially selective T2 and T2* measurement with line-scan echo-planar spectroscopic imaging. *J. Magn. Reson.* 171, 90–96.
- Chiarelli, P.A., Bulte, D.P., Wise, R., Gallician, D., Jezzard, P., 2007. A calibration method for quantitative BOLD fMRI based on hyperoxia. *NeuroImage* 37, 808–820.
- Cremillieux, Y., Ding, S., Dunn, J.F., 1998. High-resolution in vivo measurements of transverse relaxation times in rats at 7 Tesla. *Magn. Reson. Med.* 39, 285–290.
- Davis, T.L., Kwong, K.K., Weisskoff, R.M., Rosen, B.R., 1998. Calibrated functional MRI: mapping the dynamics of oxidative metabolism. *Proc. Natl. Acad. Sci. U. S. A.* 95, 1834–1839.
- de Graaf, R.A., Brown, P.B., McIntyre, S., Nixon, T.W., Behar, K.L., Rothman, D.L., 2006. High magnetic field water and metabolite proton T1 and T2 relaxation in rat brain in vivo. *Magn. Reson. Med.* 56, 386–394.
- Deistung, A., Rauscher, A., Sedlacik, J., Stadler, J., Witoszynski, S., Reichenbach, J.R., 2008. Susceptibility weighted imaging at ultra high magnetic field strengths: theoretical considerations and experimental results. *Magn. Reson. Med.* 60, 1155–1168.
- Duong, T.Q., Kim, S.G., 2000. In vivo MR measurements of regional arterial and venous blood volume fractions in intact rat brain. *Magn. Reson. Med.* 43, 393–402.
- Duong, T.Q., Kim, D.S., Ugurbil, K., Kim, S.G., 2001. Localized cerebral blood flow response at submillimeter columnar resolution. *Proc. Natl. Acad. Sci. U. S. A.* 98, 10904–10909.
- Duong, T.Q., Yacoub, E., Adriany, G., Hu, X., Ugurbil, K., Vaughan, J.T., Merkle, H., Kim, S.G., 2002. High-resolution, spin-echo BOLD, and CBF fMRI at 4 and 7 T. *Magn. Reson. Med.* 48, 589–593.
- Duong, T.Q., Yacoub, E., Adriany, G., Hu, X., Ugurbil, K., Kim, S.G., 2003. Microvascular BOLD contribution at 4 and 7 T in the human brain: gradient-echo and spin-echo fMRI with suppression of blood effects. *Magn. Reson. Med.* 49, 1019–1027.
- Duvernoy, H.M., Delon, S., Vannson, J.L., 1981. Cortical blood vessels of the human brain. *Brain Res. Bull.* 7, 519–579.
- Eichling, J.O., Raichle, M.E., Grubb Jr., R.L., Ter-Pogossian, M.M., 1974. Evidence of the limitations of water as a freely diffusible tracer in brain of the rhesus monkey. *Circ. Res.* 35, 358–364.
- Engel, S.A., Glover, G.H., Wandell, B.A., 1997. Retinotopic organization in human visual cortex and the spatial precision of functional MRI. *Cereb. Cortex* 7, 181–192.
- Fisel, C.R., Ackerman, J.L., Buxton, R.B., Garrido, L., Belliveau, J.W., Rosen, B.R., Brady, T.J., 1991. MR contrast due to microscopically heterogeneous magnetic susceptibility: numerical simulations and applications to cerebral physiology. *Magn. Reson. Med.* 17, 336–347.
- Frahm, J., Merboldt, K.-D., Hancic, W., Kleinschmidt, A., Boecker, H., 1994. Brain or vein-oxygenation or flow? On signal physiology in functional MRI of human brain activation. *NMR Biomed.* 7, 45–53.
- Fujita, N., 2001. Extravascular contribution of blood oxygenation level-dependent signal changes: a numerical analysis based on a vascular network model. *Magn. Reson. Med.* 46, 723–734.
- Gati, J.S., Menon, R.S., Ugurbil, K., Rutt, B.K., 1997. Experimental determination of the BOLD field strength dependence in vessels and tissue. *MRM* 38, 296–302.
- Gilles, P., Peto, S., Moiny, F., Mispelter, J., Cuenod, C.-A., 1995. Proton transverse nuclear magnetic relation in oxidized blood: a numerical approach. *Magn. Reson. Med.* 33, 93–100.
- Goense, J.B., Logothetis, N.K., 2006. Laminar specificity in monkey V1 using high-resolution SE-fMRI. *Magn. Reson. Imaging* 24, 381–392.
- Goense, J.B., Zappe, A.C., Logothetis, N.K., 2007. High-resolution fMRI of macaque V1. *Magn. Reson. Imaging* 25, 740–747.
- Grabill, C., Silva, A.C., Smith, S.S., Koretsky, A.P., Rouault, T.A., 2003. MRI detection of ferritin iron overload and associated neuronal pathology in iron regulatory protein-2 knockout mice. *Brain Res.* 971, 95–106.
- Grubb, R.L., Raichle, M.E., Eichling, J.O., Ter-Pogossian, M.M., 1974. The effects of changes in PaCO₂ on cerebral blood volume, blood flow, and vascular mean transit time. *Stroke* 5, 630–639.
- Haacke, E.M., Hopkins, A., Lai, S., Buckley, P., Friedman, L., Meltzer, H., Hedera, P., Friedland, R., Thompson, L., Detterman, D., Tkach, J., Lewin, J.S., 1994. 2D and 3D

- high resolution gradient-echo functional imaging of the brain: venous contributions to signal in motor cortex studies. *NMR Biomed.* 7, 54–62.
- Haacke, E.M., Cheng, N.Y., House, M.J., Liu, Q., Neelavalli, J., Ogg, R.J., Khan, A., Ayaz, M., Kirsch, W., Obenaus, A., 2005. Imaging iron stores in the brain using magnetic resonance imaging. *Magn. Reson. Imaging* 23, 1–25.
- Harel, N., Lin, J., Moeller, S., Ugurbil, K., Yacoub, E., 2006a. Combined imaging-histological study of cortical laminar specificity of fMRI signals. *NeuroImage* 29, 879–887.
- Harel, N., Ugurbil, K., Uludağ, K., Yacoub, E., 2006b. Frontiers of brain mapping using MRI. *J. Magn. Reson. Imaging* 23, 945–957.
- He, X., Yablonskiy, D.A., 2007. Quantitative BOLD: mapping of human cerebral deoxygenated blood volume and oxygen extraction fraction: default state. *Magn. Reson. Med.* 57, 115–126.
- Hoogenraad, F.G.C., Hofman, M.B.M., Pouwels, P.J.W., Reichenbach, J.R., Rombouts, S.A.R.B., Haacke, E.M., 1999. Sub-millimeter fMRI at 1.5 T: correlation of high resolution with low resolution measurements. *J. Magn. Reson. Imag.* 9, 475–482.
- Hoogenraad, F.G., Pouwels, P.J., Hofman, M.B., Reichenbach, J.R., Sprenger, M., Haacke, E.M., 2001. Quantitative differentiation between BOLD models in fMRI. *Magn. Reson. Med.* 45, 233–246.
- Jensen, J.H., Chandra, R., 2000. NMR relaxation in tissues with weak magnetic inhomogeneities. *Magn. Reson. Med.* 44, 144–156.
- Jin, T., Wang, P., Tasker, M., Zhao, F., Kim, S.G., 2006. Source of nonlinearity in echo-time-dependent BOLD fMRI. *Magn. Reson. Med.* 55, 1281–1290.
- Jochimsen, T.H., Norris, D.G., Mildner, T., Moller, H.E., 2004. Quantifying the intra- and extravascular contributions to spin-echo fMRI at 3 T. *Magn. Reson. Med.* 52, 724–732.
- Keilholz, S.D., Silva, A.C., Raman, M., Merkle, H., Koretsky, A.P., 2006. BOLD and CBV-weighted functional magnetic resonance imaging of the rat somatosensory system. *Magn. Reson. Med.* 55, 316–324.
- Kim, S.G., Hendrich, K., Hu, X., Merkle, H., Ugurbil, K., 1994. Potential pitfalls of functional MRI using conventional gradient-recalled echo techniques. *NMR Biomed.* 7, 69–74.
- Kim, T., Hendrich, K.S., Masamoto, K., Kim, S.G., 2007. Arterial versus total blood volume changes during neural activity-induced cerebral blood flow change: implication for BOLD fMRI. *J. Cereb. Blood Flow Metab.* 27, 1235–1247.
- Kiselev, V.G., Posse, S., 1999. Analytical model of susceptibility-induced MR signal dephasing: effect of diffusion in a microvascular network. *Magn. Reson. Med.* 41, 499–509.
- Kiselev, V.G., Strecker, R., Ziyeh, S., Speck, O., Hennig, J., 2005. Vessel size imaging in humans. *Magn. Reson. Med.* 53, 553–563.
- Kjolby, B.F., Ostergaard, L., Kiselev, V.G., 2006. Theoretical model of intravascular paramagnetic tracers effect on tissue relaxation. *Magn. Reson. Med.* 56, 187–197.
- Kwong, K.K., Belliveau, J.W., Chesler, D.A., Goldberg, I.E., Weisskoff, R.M., Poncelet, B.P., Kennedy, D.N., Hoppel, B.E., Cohen, M.S., Turner, R., et al., 1992. Dynamic magnetic resonance imaging of human brain activity during primary sensory stimulation. *Proc. Natl. Acad. Sci. U. S. A.* 89, 5675–5679.
- Lai, S., Hopkins, A.L., Haacke, E.M., Li, D., Wasserman, B.A., Buckley, P., Friedman, L., Meltzer, H., Hedera, P., Friedland, R., 1993. Identification of vascular structures as a major source of signal contrast in high resolution 2D and 3D functional activation imaging of the motor cortex at 1.5T: preliminary results. *Magn. Reson. Med.* 30, 387–392.
- Le Bihan, D., 2003. Looking into the functional architecture of the brain with diffusion MRI. *Nat. Rev., Neurosci.* 4, 469–480.
- Lee, S.P., Silva, A.C., Ugurbil, K., Kim, S.G., 1999. Diffusion-weighted spin-echo fMRI at 9.4 T: microvascular/tissue contribution to BOLD signal changes. *Magn. Reson. Med.* 42, 919–928.
- Lee, S.P., Silva, A.C., Kim, S.G., 2002. Comparison of diffusion-weighted high-resolution CBF and spin-echo BOLD fMRI at 9.4 T. *Magn. Reson. Med.* 47, 736–741.
- Li, T.Q., van Gelderen, P., Merkle, H., Talagala, L., Koretsky, A.P., Duyn, J., 2006. Extensive heterogeneity in white matter intensity in high-resolution T2*-weighted MRI of the human brain at 7.0 T. *NeuroImage* 32, 1032–1040.
- Logothetis, N.K., Pauls, J., Augath, M., Trinath, T., Oeltermann, A., 2001. Neurophysiological investigation of the basis of the fMRI signal. *Nature* 412, 150–157.
- Lu, H., van Zijl, P.C., 2005. Experimental measurement of extravascular parenchymal BOLD effects and tissue oxygen extraction fractions using multi-echo VASO fMRI at 1.5 and 3.0 T. *Magn. Reson. Med.* 53, 808–816.
- Lu, H., Golay, X., Pekar, J.J., Van Zijl, P.C., 2003. Functional magnetic resonance imaging based on changes in vascular space occupancy. *Magn. Reson. Med.* 50, 263–274.
- Lu, H., Golay, X., Pekar, J.J., Van Zijl, P.C., 2004. Sustained poststimulus elevation in cerebral oxygen utilization after vascular recovery. *J. Cereb. Blood Flow Metab.* 24, 764–770.
- Lu, H., Scholl, C.A., Zuo, Y., Stein, E.A., Yang, Y., 2007. Quantifying the blood oxygenation level dependent effect in cerebral blood volume-weighted functional MRI at 9.4T. *Magn. Reson. Med.* 58, 616–621.
- Menon, R.S., Ogawa, S., Tank, D.W., Ugurbil, K., 1993. 4 Tesla gradient recalled echo characteristics of photic stimulation – induced signal changes in the human primary visual cortex. *Magn. Reson. Med.* 30, 380–387.
- Mitsumori, F., Watanabe, H., Takaya, N., Garwood, M., 2007. Apparent transverse relaxation rate in human brain varies linearly with tissue iron concentration at 4.7 T. *Magn. Reson. Med.* 58, 1054–1060.
- Moon, C.H., Fukuda, M., Park, S.H., Kim, S.G., 2007. Neural interpretation of blood oxygenation level-dependent fMRI maps at submillimeter columnar resolution. *J. Neurosci.* 27, 6892–6902.
- Norris, D.G., Zysset, S., Mildner, T., Wiggins, C.J., 2002. An investigation of the value of spin-echo-based fMRI using a Stroop color-word matching task and EPI at 3 T. *NeuroImage* 15, 719–726.
- Obata, T., Liu, T.T., Miller, K.L., Luh, W.M., Wong, E.C., Frank, L.R., Buxton, R.B., 2004. Discrepancies between BOLD and flow dynamics in primary and supplementary motor areas: application of the balloon model to the interpretation of BOLD transients. *NeuroImage* 21, 144–153.
- Ogawa, S., Lee, T.M., Kay, A.R., Tank, D.W., 1990. Brain magnetic resonance imaging with contrast dependent on blood oxygenation. *Proc. Natl. Acad. Sci. U. S. A.* 87, 9868–9872.
- Ogawa, S., Tank, D.W., Menon, R., Ellermann, J.M., Kim, S.G., Merkle, H., Ugurbil, K., 1992. Intrinsic signal changes accompanying sensory stimulation: functional brain mapping with magnetic resonance imaging. *Proc. Natl. Acad. Sci. U. S. A.* 89, 5951–5955.
- Ogawa, S., Menon, R.S., Tank, D.W., Kim, S.G., Merkle, H., Ellermann, J.M., Ugurbil, K., 1993. Functional brain mapping by blood oxygenation level-dependent contrast magnetic resonance imaging. A comparison of signal characteristics with a biophysical model. *Biophys. J.* 64, 803–812.
- Oja, J.M.E., Gillen, J., Kauppinen, R.A., Kraut, M., Zijl, P.C.M.v., 1999. Venous blood effects in spin-echo fMRI of human brain. *Magn. Reson. Med.* 42, 617–626.
- Parkes, L.M., Schwarzbach, J.V., Bouts, A.A., Deckers, R.H., Pullens, P., Kerskens, C.M., Norris, D.G., 2005. Quantifying the spatial resolution of the gradient echo and spin echo BOLD response at 3 Tesla. *Magn. Reson. Med.* 54, 1465–1472.
- Paulson, O.B., Hertz, M.M., Bolwig, T.G., Lassen, N.A., 1977. Filtration and diffusion of water across the blood-brain barrier in man. *Microvasc. Res.* 13, 113–124.
- Pawlik, G., Rackl, A., Bing, R.J., 1981. Quantitative capillary topography and blood flow in the cerebral cortex of cats: an in vivo microscopic study. *Brain Res.* 208, 35–58.
- Peters, A.M., Brookes, M.J., Hoogenraad, F.G., Gowland, P.A., Francis, S.T., Morris, P.G., Bowtell, R., 2007. T2* measurements in human brain at 1.5, 3 and 7 T. *Magn. Reson. Imaging* 25, 748–753.
- Ramani, A., Jensen, J.H., Helpert, J.A., 2006. Quantitative MR imaging in Alzheimer disease. *Radiology* 241, 26–44.
- Ress, D., Glover, G.H., Liu, J., Wandell, B., 2007. Laminar profiles of functional activity in the human brain. *NeuroImage* 34, 74–84.
- Shmuel, A., Yacoub, E., Chaimow, D., Logothetis, N.K., Ugurbil, K., 2007. Spatio-temporal point-spread function of fMRI signal in human gray matter at 7 Tesla. *NeuroImage* 35, 539–552.
- Silvennoinen, M.J., Clingman, C.S., Golay, X., Kauppinen, R.A., van Zijl, P.C., 2003. Comparison of the dependence of blood R2 and R2* on oxygen saturation at 1.5 and 4.7 Tesla. *Magn. Reson. Med.* 49, 47–60.
- Smirnakis, S.M., Schmid, M.C., Weber, B., Tolias, A.S., Augath, M., Logothetis, N.K., 2007. Spatial specificity of BOLD versus cerebral blood volume fMRI for mapping cortical organization. *J. Cereb. Blood Flow Metab.* 27, 1248–1261.
- Song, A.W., Wong, E.C., Bandettini, P.A., Hyde, J.S., 1994. The effect of diffusion weighting on task-induced functional MRI. Second Meeting, Society of Magnetic Resonance, San Francisco, p. 643.
- Song, A.W., Wong, E.C., Jesmanowicz, A., Tan, S.G., Hyde, J.S., 1995. Diffusion weighted fMRI at 1.5 T and 3 T. Third Meeting, Society of Magnetic Resonance, Nice, France, p. 457.
- Song, A.W., Wong, E.C., Tan, S.G., Hyde, J.S., 1996. Diffusion weighted fMRI at 1.5 T. *Magn. Reson. Med.* 35, 155–158.
- Song, A.W., Harshbarger, T., Li, T., Kim, K.H., Ugurbil, K., Mori, S., Kim, D.S., 2003. Functional activation using apparent diffusion coefficient-dependent contrast allows better spatial localization to the neuronal activity: evidence using diffusion tensor imaging and fiber tracking. *NeuroImage* 20, 955–961.
- Spees, W.M., Yablonskiy, D.A., Oswood, M.C., Ackerman, J.J., 2001. Water proton MR properties of human blood at 1.5 Tesla: magnetic susceptibility, T(1), T(2), T*(2), and non-Lorentzian signal behavior. *Magn. Reson. Med.* 45, 533–542.
- Stanisz, G.J., Odobina, E.E., Pun, J., Escaravage, M., Graham, S.J., Bronskill, M.J., Henkelman, R.M., 2005. T1, T2 relaxation and magnetization transfer in tissue at 3T. *Magn. Reson. Med.* 54, 507–512.
- Sukstanskii, A.L., Yablonskiy, D.A., 2001. Theory of FID NMR signal dephasing induced by mesoscopic magnetic field inhomogeneities in biological systems. *J. Magn. Reson.* 151, 107–117.
- Thulborn, K.R., Waterton, J.C., Matthews, P.M., Radda, G.K., 1982. Oxygenation dependence of the transverse relaxation time of water protons in whole blood at high field. *Biochim. Biophys. Acta* 714, 265–270.
- Turner, R., 2002. How much cortex can a vein drain? Downstream dilution of activation-related cerebral blood oxygenation changes. *NeuroImage* 16, 1062–1067.
- Ugurbil, K., Toth, L., Kim, D.S., 2003. How accurate is magnetic resonance imaging of brain function? *Trends Neurosci.* 26, 108–114.
- van Zijl, P.C., Eleff, S.M., Ulatowski, J.A., Oja, J.M., Ulug, A.M., Traystman, R.J., Kauppinen, R. A., 1998. Quantitative assessment of blood flow, blood volume and blood oxygenation effects in functional magnetic resonance imaging. *Nat. Med.* 4, 159–167.
- Vanzetta, I., Hildesheim, R., Grinvald, A., 2005. Compartment-resolved imaging of activity-dependent dynamics of cortical blood volume and oximetry. *J. Neurosci.* 25, 2233–2244.
- Vovenko, E., 1999. Distribution of oxygen tension on the surface of arterioles, capillaries and venules of brain cortex and in tissue in normoxia: an experimental study on rats. *Pflügers Arch.* 437, 617–623.
- Weber, B., Keller, A.L., Reichold, J., Logothetis, N.K., 2008. The microvascular system of the striate and extrastriate visual cortex of the macaque. *Cereb. Cortex.*
- Weigel, M., Hennig, J., 2006. Contrast behavior and relaxation effects of conventional and hypercho-turbo spin echo sequences at 1.5 and 3 T. *Magn. Reson. Med.* 55, 826–835.
- Weisskoff, R.M., Kihne, S., 1992. MRI susceptometry: image-based measurement of absolute susceptibility of MR contrast agents and human blood. *Magn. Reson. Med.* 24, 375–383.
- Weisskoff, R.M., Hoppel, B.J., Rosen, B.R., 1992. Signal changes in dynamic contrast studies: theory and experiment in vivo. *JMRI* 2(P) [Abstr.], 77.
- Weisskoff, R.M., Boxerman, J.L., Zuo, C.S., Rosen, B.R., 1993. Endogenous susceptibility contrast: principles of relationship between blood oxygenation and MR signal change. *Functional MRI of the Brain. Society of Magnetic Resonance in Medicine, Berkeley, p. 103.*
- Weisskoff, R.M., Zuo, C.S., Boxerman, J.L., Rosen, B.R., 1994. Microscopic susceptibility variation and transverse relaxation: theory and experiment. *Magn. Reson. Med.* 31, 601–610.

- Yablonskiy, D.A., Haacke, E.M., 1994. Theory of NMR signal behavior in magnetically inhomogeneous tissues: the static dephasing regime. *Magn. Reson. Med.* 32, 749–763.
- Yacoub, E., Duong, T.Q., Van De Moortele, P.F., Lindquist, M., Adriany, G., Kim, S.G., Ugurbil, K., Hu, X., 2003. Spin-echo fMRI in humans using high spatial resolutions and high magnetic fields. *Magn. Reson. Med.* 49, 655–664.
- Yacoub, E., Van De Moortele, P.F., Shmuel, A., Ugurbil, K., 2005. Signal and noise characteristics of Hahn SE and GE BOLD fMRI at 7 T in humans. *NeuroImage* 24, 738–750.
- Yacoub, E., Ugurbil, K., Harel, N., 2006. The spatial dependence of the poststimulus undershoot as revealed by high-resolution BOLD- and CBV-weighted fMRI. *J. Cereb. Blood Flow Metab.* 26, 634–644.
- Yacoub, E., Shmuel, A., Logothetis, N., Ugurbil, K., 2007. Robust detection of ocular dominance columns in humans using Hahn Spin Echo BOLD functional MRI at 7 Tesla. *NeuroImage* 37, 1161–1177.
- Yacoub, E., Harel, N., Ugurbil, K., 2008. High-field fMRI unveils orientation columns in humans. *Proc. Natl. Acad. Sci. U. S. A.* 105, 10607–10612.
- Zhao, F., Wang, P., Kim, S.G., 2004. Cortical depth-dependent gradient-echo and spin-echo BOLD fMRI at 9.4T. *Magn. Reson. Med.* 51, 518–524.
- Zhao, F., Wang, P., Hendrich, K., Ugurbil, K., Kim, S.G., 2006. Cortical layer-dependent BOLD and CBV responses measured by spin-echo and gradient-echo fMRI: insights into hemodynamic regulation. *NeuroImage* 30, 1149–1160.
- Zhao, J.M., Clingman, C.S., Narvainen, M.J., Kauppinen, R.A., van Zijl, P.C., 2007. Oxygenation and hematocrit dependence of transverse relaxation rates of blood at 3T. *Magn. Reson. Med.* 58, 592–597.

Glossary

- GRE*: Gradient-recalled echo
SE: Single-refocused spin echo
IV: Intravascular
EV: Extra-vascular
 $\Delta\chi$: Susceptibility
S: MRI signal
 R_2 : Relaxation rate
 T_2 : Relaxation time
TE: Echo time
 ϕ : Relative spin density
RF: Radiofrequency
Deoxy-Hb: Deoxygenated hemoglobin
Y: Oxygen saturation
CBV: Cerebral blood volume
CBF: Cerebral blood flow
Hct: Hematocrit
R: Radius
CNR: Contrast-to-Noise-Ratio
ODC: Ocular dominance column
OC: Orientation column